A COMBINED PIEZOELECTRIC COMPOSITE ACTUATOR AND ITS APPLICATION TO WING/BLADE TIPS

A Thesis
Presented to
The Academic Faculty

By

Kwangtae Ha

In Partial Fulfillment
of the Requirements for the Degree
Doctor of Philosophy in the
School of Aerospace Engineering

Georgia Institute of Technology

December 2005

A COMBINED PIEZOELECTRIC COMPOSITE ACTUATOR AND ITS APPLICATION TO WING/BLADE TIPS

Approved by:

Dr. D. Stefan Dancila, Advisor
School of Aerospace Engineering
Georgia Institute of Technology

Dr. Massimo Ruzzene
School of Aerospace Engineering
Georgia Institute of Technology

Dr. Erian A. Armanios
School of Aerospace Engineering
Georgia Institute of Technology

Dr. Christopher S. Lynch
School of Mechanical Engineering
Georgia Institute of Technology

Dr. Olivier A. Bauchau
School of Aerospace Engineering
Georgia Institute of Technology

Date Approved: November 28, 2005

To my family:

My wife, Simbackhwa Lee

My baby, Gundam Ha

For their love, encouragement, understanding and believing.

A C K N O W L E D G M E N T S

First and foremost, I would like to thank God for blessing me and allowing me such opportunities as to initiate and complete my Ph.D.

I would like to express my most profound gratitude and sincere appreciation to my thesis advisor, Professor D. Stefan Dancila, for his guidance, encouragement, and support which he has generously provided throughout the preparation of this work.

I am truly grateful to Professor Erian A. Armanios and Professor Olivier A. Bauchau for their advice and assistance. I am indebted to both for many enlightening discussions. I wish to extend my special thanks to Professors Massimo Ruzzene and Professor Christopher S. Lynch for serving on the thesis committee and for their useful comments.

I would also like to thank all of my colleagues for their help and supports.

Much appreciation and love is extended to all of my family and friends. I would like to especially acknowledge my parents, Jong-Bok Ha and Myung-Sook Shin and my parents-in-law, Chun-Hyo Lee and Jum-Ok Cho, for their continued understanding, encouragement and love throughout this journey.

Most importantly, I would like to express my gratitude to my wife, Simbackhwa Lee, and future baby, Gundam, for their love, sacrifice, and encouragement. Thank you. I love you all.

TABLE OF CONTENTS

Acknowledgments ..... **iv**

List of Tables ..... **vii**

List of Figures ..... **viii**

List of Symbols ..... **xiii**

Summary ..... **xviii**

Chapter I Introduction **1**

1.1 Objective 1

1.2 Background 1

1.3 Overview 5

Chapter II Literature Survey **6**

2.1 Smart Materials 6

2.2 On-Blade Active Systems for Vibration Reduction in Rotorcraft 14

2.3 Elastically Tailored Composite Structure 19

Chapter III A Combined Piezoelectric Composite Actuator Configuration and Modeling **21**

3.1 Active Blade Tip Configuration 21

3.2 Modeling Approach 26

3.3 Characterization of a Coiled Bender Piezoelectric Actuator 27

3.4 Modeling of a Modified Star Shape Cross Sectional Beam 31

3.5 Characterization of a Combined Piezoelectric Composite Actuator 46

Chapter IV Application of a Combined Piezoelectric Composite Actuator to Wing/Blade Tips 50

4.1 Aerodynamic Loading 50

4.2 Centrifugal Loading at the Blade Tip 52

4.3 Equilibrium Equation at the Blade Tip 55

4.4 Numerical Results 57

Chapter V Conclusions and Recommendations for Future Work 84

Appendix A Analysis of a Thin Walled Beam with Constant Axial Load and Tip Torque 88

References 92

Vita 101

LIST OF TABLES

Table II.1 Comparison of Relevant Smart Materials' Properties 7

Table III.1 Material Properties.....35

Table III.2 Geometric Characteristics.....35

Table III.3 Comparison of Predictions.....36

Table III.4 Geometric Properties of Combined Piezoelectric Composite Actuator 48

Table IV.1 Piezoelectric Material Properties.....58

Table IV.2 Geometric Properties of a Starbeam.....58

Table IV.3 Main Wing/Blade Model's Properties.....61

Table IV.4 10% Span Wing/Blade Tip Model's Properties 61

Table IV.5 Blade Tip Deflection Range for X_h=0.0% chord length (starbeam).....68

Table IV.6 Blade Tip Deflection Range for X_h=1.0% chord length (starbeam).....72

Table IV.7 Blade Tip Deflection Range for X_h=1.5% chord length (starbeam).....72

Table IV.8 Geometric Properties of a Modified Starbeam.....73

Table IV.9 Blade Tip Deflection Range for X_h=0.0% chord length
(modified starbeam).....76

Table IV.10 Blade Tip Deflection Range for X_h=1.5% chord length
(modified starbeam).....77

LIST OF FIGURES

Figure II.1 Various configurations of piezoceramic actuators....9

Figure II.2 Active Fiber Composite (AFC)....16

Figure II.3 Principle operation of free tip....18

Figure III.1 A combined piezoelectric composite actuator configuration....22

Figure III.2 Applications of a combined piezoelectric composite actuator as tension-torsion hinge bar actuator....22

Figure III.3 Helicoidal bimorph piezoelectric actuators....24

Figure III.4 Geometry of a coiled bender actuator....28

Figure III.5 Star shape cross sectional configurations....31

Figure III.6 Redistribution of a circular cross sectional area (star shape and modified star shape configurations)....31

Figure III.7 A geometric configuration of a modified starbeam....32

Figure III.8 ABAQUS FEM model of a modified starbeam....33

Figure III.9 SVBT cross sectional FE model....34

Figure III.10 Variation of GJ ratio....38

Figure III.11 Variation of EI ratio....39

Figure III.12 Optimal EI ratio for N=3....40

Figure III.13 Optimal EI ratio for N=4....41

Figure III.14 Surface plot of GJ ratio variation for N=3....41

Figure III.15 Surface plot of EI ratio variation for N=3 42
Figure III.16 Variation of GJ ratio with N 42
Figure III.17 Variation of EI ratio with N 43
Figure III.18 A modified starbeam subjected to several types of loading 44
Figure III.19 A modified starbeam subjected to combined loading 47
Figure III.20 Free rotational angle of a combined actuator 49
Figure III.21 Effects of applied voltage and axial load on the tip angle of a combined actuator 49
Figure IV.1 Local reference system for blade tip cross section 53
Figure IV.2 Free body diagram of free tip 56
Figure IV.3 Maximum twisting angle vs. actuator width 59
Figure IV.4 Maximum twisting angle vs. geometric parameters with 40
Figure IV.5 Wing tip deflection angle with the pitch angle of 0 degree with respect to tip Mach number (starbeam) 62
Figure IV.6 Wing tip deflection angle with the pitch angle of 4 degree with respect to tip Mach number (starbeam) 62
Figure IV.7 DYMORE model of half span wing 63
Figure IV.8 Maximum deflection angle of a wing tip with the pitch angle of 0 degree with respect to applied voltage and Mach number 64
Figure IV.9 Maximum deflection angle of a wing tip with the pitch angle of 4 degree with respect to applied voltage and Mach number 64
Figure IV.10 DYMORE model of rotorcraft blade with moving tip 65
Figure IV.11 Schematic design of blade tip model in DYMORE 66

Figure IV.12 Blade tip deflection angle with hinge location of 0.0% chord length and pitch angle of 0 degree with respect to tip Mach number (starbeam) 67
Figure IV.13 Blade tip deflection angle with hinge location of 0.0% chord length and pitch angle of 4 degree with respect to tip Mach number (starbeam) 68
Figure IV.14 Blade tip deflection angle with hinge location of 1.0% chord length and pitch angle of 0 degree with respect to tip Mach number (starbeam) 70
Figure IV.15 Blade tip deflection angle with hinge location of 1.0% chord length and pitch angle of 4 degree with respect to tip Mach number (starbeam) 70
Figure IV.16 Blade tip deflection angle with hinge location of 1.5% chord length and pitch angle of 0 degree with respect to tip Mach number (starbeam) 71
Figure IV.17 Blade tip deflection angle with hinge location of 1.5% chord length and pitch angle of 4 degree with respect to tip Mach number (starbeam) 71
Figure IV.18 Blade tip deflection angle with hinge location of 0.0% chord length and pitch angle of 0 degree with respect to tip Mach number (modified starbeam).....74
Figure IV.19 Blade tip deflection angle with hinge location of 0.0% chord length and pitch angle of 4 degree with respect to tip Mach number (modified starbeam).....75
Figure IV.20 Blade tip deflection angle with hinge location of 1.5% chord length and pitch angle of 0 degree with respect to tip Mach number (modified starbeam).....75

Figure IV.21 Blade tip deflection angle with hinge location of 1.5% chord length and pitch angle of 4 degree with respect to tip Mach number (modified starbeam).....76
Figure IV.22 Blade tip deflection angle with hinge location of 1.5% chord length and pitch angle of 0 degree with respect to ratio of modified starbeam to blade length 78
Figure IV.23 Blade tip deflection angle with hinge location of 1.5% chord length and pitch angle of 4 degree with respect to ratio of modified starbeam to blade length 78
Figure IV.24 Blade tip deflection angle with 0.26 valued tip Mach number and pitch angle of 0 degree with respect to hinge location of modified starbeam 79
Figure IV.25 Blade tip deflection angle with 0.26 valued tip Mach number and pitch angle of 4 degree with respect to hinge location of modified starbeam 80
Figure IV.26 Inertia effect to tip deflection angle with hinge location of 1.5% chord length and pitch angle of 0 degree with respect to tip Mach number (modified starbeam).....81
Figure IV.27 Inertia effect to tip deflection angle with hinge location of 1.5% chord length and pitch angle of 4 degree with respect to tip Mach number (modified starbeam).....81
Figure IV.28 Blade tip deflection angle with hinge location of 1.5% chord length and 0.26 valued tip Mach number with respect to the pitch angle of attack of blade.....82

Figure IV.29 Comparison of stiffness ratio of torsional stiffness due to centrifugal force to elastic stiffness of starbeam with that of a modified starbeam with hinge location of 1.5% chord length and pitch angle of 4 degree 83
Figure A.1 Undeformed (solid line) and deformed (dot line) configurations of the thin walled beam 89

LIST OF SYMBOLS

Capital letters

A	Cross sectional area
AR	Aspect ratio (=c/R)
C_l^α	Lift curve slope
C_T	Rotor thrust coefficient
E	Elastic (Young's) modulus
E_c	1-1 elastic stiffness constant of the piezoelectric material
E_d	Depolarization electric field
$(EA)_s$	Axial stiffness of the star/modified star shaped beam
$(EI)_s$	Bending stiffness of star/modified shaped beam
E_{11}	Engineering constant of composite material in the 1-1 direction
E_{22}	Engineering constant of composite material in the 2-2 direction
E_3	Applied 3-direction electric field
F	Applied constant axial load in the y direction
$\vec{F}$	Force vector acting on the blade tip mass
$\vec{F}_{CF}$	Centrifugal force vector acting on the blade tip mass center
F_y	Force component in the y direction
$F(\lambda, r)$	Prandtl's circulation loss function

G	Shear modulus
$(GJ)_s$	Torsional stiffness of star/modified shaped beam
G_{12}	Engineering constant of composite material in the 1-2 direction
G_{13}	Engineering constant of composite material in the 1-3 direction
G_{23}	Engineering constant of composite material in the 2-3 direction
I	Second moment of area
I_{NL}	Nonlinear term related to coupling of tip torque and axial load
I_s	Second moment of area of star/modified shaped beam
J	Torsional constant
J_{XX}^{C}	Pitching inertia of tip mass expressed about the mass center
K_{coil}	Overall torsional stiffness of the coiled actuator
K_{el}	Overall elastic torsional stiffness of star/modified shaped beam
K_F	Apparent torsional stiffness of star/modified shaped beam due to coupling of tip torque and axial load
K_{NL}	Nonlinear term identified as due to trapeze effect
L_{aero}	Total lift loading over the active blade tip
L_c	Length of coiled bender actuator
M_{aero}	Aerodynamic pitching moment (=$X_h L_{aero}$)
M_c	Cross-sectional coiled bender blocked moment
$\vec{M}_y$	Flattening moment (Tennis-racquet effect)
M_{Tip}	Tip Mach number of the wing/blade

N_b Number of blades

N_s Number of strips (arms)

R Wing/blade length

$\vec{R}$ Position vector of wing/blade tip mass center

T Applied constant tip torque in the y-direction

T_y Tip torque component in the y-direction

U_y Displacement component in the y-direction

V Applied control voltage

X_c Distance of mass center of the wing/blade tips from leading edge toward trailing edge

X_h Hinge location from the aerodynamic center toward trailing edge

Y_c Distance of mass center of the wing/blade tips from hub toward wing/blade tips

Lower case letters

a Speed of sound

b_c Width of coiled bender actuator

b_s Radius of the star/modified cross section

c Chord length

d Diameter of the circular cross section

d_{15} Piezoelectric strain constant in the 5-axis induced due to a unit applied field in the 1-axis

d_{31} Piezoelectric strain constant in the 1-axis induced due to a unit applied

	field in the 3-axis
d_{33}	Piezoelectric strain constant in the 3-axis induced due to a unit applied field in 3-axis
$\vec{e}_X$	Unit vector in the X-direction in the global reference system
$\vec{e}_Y$	Unit vector in the Y-direction in the global reference system
$\vec{e}_Z$	Unit vector in the Z-direction in the global reference system
k_c	Change in principal curvature of the shell surface of coiled bender actuator
m	Mass of wing/blade tips
r	Nondimensional length of blade (=y/R)
r_c	Midplane radius of coiled bender actuator
r_0	Initial midplane radius of coiled bender actuator
t_c	Thickness of coiled bender actuator
t_s	Thickness of the star/modified shaped beam

Capital Greek symbols

Σ	Total coil wrapping angle of coiled bender actuator
Ω	Rotor angular velocity
$\vec{\Omega}$	Angular velocity vector

Lower case Greek symbols

α	Extension angle of the side arc
β	Collective pitch angle
ε_y	Strain component in the y-direction
ϕ_s	Twist rate of star/modified shaped beam

η	Nondimensional aspect ratio $(=\frac{t_s}{b_s})$
φ	Nondimensional arc angle of modified starbeam $(=\frac{N_s\alpha}{\pi})$
φ_{opt}	Optimal arc angle of modified starbeam
κ_1	Geometric configuration parameter
λ	Non-uniform inflow variable
μ	Current coil angle of coiled bender actuator
v_{12}	1-2 Poisson's ratio of composite material
θ	Deflected angle of wing/blade tip
θ_c	Free rotation angle of coiled bender actuator
θ_s	Tip twist angle of star/modified shaped beam
ρ	Air density at the sea level
σ	Rotor solidity
σ_y	Stress component in the y-direction

Subscript

s	Star/modified shaped beam
coil	Coiled bender actuator
circular	Circular cross section

SUMMARY

A novel combined piezoelectric-composite actuator configuration is proposed and analytically modeled in this work. The actuator is a low complexity, active compliant mechanism obtained by coupling a modified star cross sectional configuration composite beam with a helicoidal bimorph piezoelectric actuator coiled around it. The modified star beam is tailored and optimized to achieve increased torsional compliance and bending stiffness at given constant axial stiffness. The coiled piezoelectric actuator is designed to directly generate finite rotation output without the need for mechanisms to amplify the piezoelectric displacement output and/or convert linear output to rotational output. The proposed combined piezoelectric-composite actuator is compact and is a good candidate for use among other applications as a hinge tension-torsion bar actuator for a helicopter rotor blade flap or blade tip. For such cases the modified star composite beam carries the centrifugal loads of the flap or blade tip, and those of the coiled actuator, thereby eliminating the need for a thrust bearing. Consequently, friction/sticktion and backlash effects that represent difficulties commonly encountered by other induced strain blade actuation configurations are eliminated. Another good candidate application for the proposed combined piezoelectric composite actuator is that of mirror rotational positioning.

As applications of the actuator models developed, the steady state response of a helicopter blade tip and of a wing tip supported by a combined piezoelectric composite

actuator were investigated. In the wing tip case, the tip deflection angle is determined by the aerodynamic moment depending on the hinge position of the actuator along the chord and applied voltage because there is no centrifugal force.

For an active blade tip subject to incompressible flow and 2D quasi steady airloads, its twist angle is related not only to aerodynamic moment and applied voltage but also to coupling terms due to the trapeze effect and the tennis racquet effect. Results show the benefit of hinge position aft of the aerodynamic center, such that the blade tip response is amplified by airloads. In contrast with this effect, results also show that the centrifugal effects and inertial effects cause an amplitude reduction in the response. Summation of these effects determines the overall blade tip response. The results for a certain hinge position of X_h=1.5% chord aft of the quarter chord point proves that the tip deflection target design range of $\beta \in [-2,+2]$ can be achieved for all pitch angle configurations chosen.

CHAPTER I

INTRODUCTION

1.1 OBJECTIVE

The objective of the present research is to propose and model a novel combined piezoelectric composite actuator system with applicability to among others, rotor blades for airload control and to mirror rotary positioning. Each component comprising the combined actuator, a star shaped composite beam and a helicoidal piezoelectric actuator, will be analyzed and modeled separately. As an application, the steady state response of active blade/wing tips utilizing such a composite-piezoelectric actuator is then studied analytically and computationally.

1.2 BACKGROUND

In recent years researchers have been investigating the applications of new materials to existing engineering systems in an effort to improve their performance, for example, in order to reduce vibrations and noise in helicopters. Helicopter vibrations and noise exist in all flight conditions mainly due to the unsteady working environment of the blades. This results from interactions between the highly unsteady aerodynamic loads induced by the rotor blades and from aerodynamic phenomena like stall on the retreating blade and transonic effects on the advancing blade, which lead among others to pilot

fatigue and poor ride quality. As a result, a high priority has been placed on reducing or eliminating these vibratory loads, and much work has been performed to develop various passive and active methods and mechanisms for achieving this task (Reichart [1]; Loewy [2]).

Traditional passive approaches to vibration reduction, such as absorbers and isolators, or blade and airframe structural optimization, have generally proven to not be effective and/or efficient enough to realize the desired comfort level of "jet-smooth" rotorcraft flight. During the past several decades, active control of vibration has been aggressively investigated by many organizations.

The development of effective, efficient and reliable rotorcraft on-blade actuation technologies is of great interest for application to direct flight control, vibration reduction, and Blade Vortex Interaction (BVI) noise reduction via Individual Blade Control (IBC) and/or Higher Harmonic Control (HHC). Several technical requirements contribute to the increased level of difficulty of this task: i) reliable transmission of actuation power from the fixed to the rotating frame, ii) actuation system operation in an environment characterized by high accelerations (both centripetal and due to maneuver and vibrations), iii) reduced weight penalty associated with the actuation system, and iv) high actuation bandwidth to allow upwards of 5-6/rev actuation.

On-blade actuation approaches using active flaps, active blade tips, and active blade twist have been explored.

Difficulties associated with hydraulic slip ring sealing, the typically high weight penalty of hydraulic system and their limited bandwidth have virtually ruled out the practical use of servo-hydraulic devices for on-blade actuation.

The use of electromagnetic/electrodynamic actuators for helicopter rotor blade actuation has been explored by Fink *et. al.* [3] and by Duvernier *et. al.* [4]. Such actuators are characterized by higher energy densities compared to piezoelectric counterparts and are capable of generating substantially constant actuation force/moment through the entire stroke range. However, they require high actuation electric currents and power, and generate significant heating that needs to be dissipated. Additionally, the lack of stiffness when the actuator is not energized (such as may be the case due to actuation control system failure) raises concerns for loss of stability of the actuated flap and potentially of the rotor system.

Induced strain active material actuators (piezoelectric, magnetostrictive and shape memory alloy based) have received special attention. In particular, piezoelectric actuators have been considered due to convenient actuation via applied electric field, and due to fast response [5-33].

Active twist composite blades using distributed, embedded piezoelectric actuators in fiber form (Wilkie *et. al.* [32], Cesnik and Shin [33]) are represented as approaching the ideal model of a morphing structure. The impetus for morphing structures originates in the biological realm, with a bird wing or a human hand providing examples of outstanding degrees of morphing. However, it should be recognized that the morphing action involved in such examples is generated by the use of muscles to reconfigure a system consisting of bones connected by joints, i.e. a mechanism. The case of a muscle embedded into a bone in order to deform it is not encountered. This analogy may be useful when considering the lack of effectiveness of embedded piezoelectric actuators in generating structural morphing. The high nominal stiffness of the base structure and the

limited authority of piezoelectric actuators result in limited overall actuation capability. Additionally, the high density of piezoelectric materials results in a significant weight penalty for this approach. Reduced reliability of embedded actuator patches has also been reported [34-35].

Other approaches have used piezoelectric actuators to control a mechanism that deflects a flap or a blade tip. The mechanisms involved perform one or both of the following functions: i) displacement output amplification ([Paine and Chaudry [36] and Giurgiutiu, Chaudry, and Rogers [37]) (e.g. the X-frame in the case of piezoelectric stack ([Prechtl and Hall [26])), ii) linear output to rotary output conversion, in order to generate flap or blade tip rotation. Such mechanisms are, however, negatively affected by the presence of high centrifugal forces typical of a rotor blade environment, resulting in friction/sticktion that degrades performance.

A solution to the problem caused by centrifugal loads on the flap or blade tip consists in the replacement of the thrust bearing by a tension-torsion bar (Bernhard and Chopra [15-17], Straub and King [28], Straub *et. al.* [29, 31], Straub and Charles [30]). The generation of rotation by using a compliant, tailored bend-twist coupled structure has been explored by Bernhard and Chopra [14-17]. The direct generation of rotary actuator output has been also investigated by Glazounov, Zhang, and Kim [38-39], Kim *et. al.* [40-42], and Kim, Glazounov, and Zhang [43], using shear mode deformation in piezoelectric tubes.

The detailed literature review of the on-blade actuation system for vibration reduction and development and testing of piezoelectric material based smart actuators is given in the following chapter.

1.3 OVERVIEW

The remaining chapters of this thesis are organized as follows. Chapter II will present a literature survey on actuation methodologies. The configuration and analytical modeling for the combined composite-piezoelectric actuator will be presented in Chapter III. Application of the combined composite-piezoelectric actuator to rotorcraft blade tip and recommendations for future work will be discussed in Chapter IV and Chapter V, respectively.

CHAPTER II

LITERATURE SURVEY

A literature survey of prior research relevant to the current study is given in this chapter starting from smart materials, in particular piezoelectric materials. The second part describes several studies of vibration reduction using on-blade actuation system. The last part addresses elastically tailored composite structures

2.1 SMART MATERIALS

Development of smart materials and structures is a rapidly emerging field in engineering. The motivation to develop smart materials and structures comes from the desire to provide products with life-like functions that integrate sensing, actuating, control, and intelligence (Newnham and Ruschau [44]). Recent advances in smart material technology have enabled the development of devices which can serve as both sensors and actuators. When these devices are integrated into a structure together with a controller it becomes “smart”, i.e., it can sense changes in its environment and adapt to those changes. However, a major barrier in the design of smart structures is that current actuation devices are limited in their displacement output capability. There is an ongoing need in the field of smart structures for actuators with improved output stroke performance.

Numerous induced strain actuators have been designed using smart materials (Loewy [45]). These actuators include piezoceramic stacks and bimorphs, where an

applied voltage produces a mechanical strain; shape memory alloy, where a temperature change produces significant strain from expansion and contraction of the alloy superstructure; magnetostrictive devices such as Terfenol, where a mechanical strain is induced by a magnetic field; and electrostrictive devices, where a mechanical strain is induced by an electric field (Culshaw [46] and Banks [47]). Typical values and/or orders of magnitude for the relevant properties of each of these materials are briefly compared in Table II. 1.

Table II. 1. Comparison of Relevant Smart Materials' Properties

Materials	PZT-5H	PVDF	Terfenol	Nitinol
Actuation Mechanism	Piezoelectric (ceramic)	Piezoelectric (polymer)	Magneto-strictive	Shape Memory Alloy
Maximum Free strain ($\mu\varepsilon$)	10^3	7×10^2	2×10^3	2×10^4
Modulus (*GPa*)	62	3	40	78
Density (kg/m^3)	7500	1780	9250	6450
Bandwidth (*Hz*) (Order of magnitude)	10^3	10^3	10^2	10^0

2.1.1 PIEZOCERAMIC ACTUATORS

Among smart materials piezoceramic ones are of wider use. Pierre and Jacques Curie discovered piezoelectricity in the 1880's. Piezoelectric materials undergo strain when an electric field is applied (converse piezoelectric effect) and produce an electric charge with the application of strain (direct piezoelectric effect). This reversible effect makes piezoelectric materials ideal for use as both actuators and sensors. Under an applied field, these materials generate low strains over a wide range of actuation frequency. The most widely used piezoceramics (such as lead (Pb) zirconate (Zr) titanate (Ti) or PZT) are available in the form of thin sheets, which can be readily embedded or attached to various structures (Park, Waltz, and Chopra [48]). Bi-morphs or bending actuators are also commercially available, and are formed from two layers of these materials bonded to a thin shim (typically of brass) located in between. If opposite strains are induced through electrical field in the two plates, a bending effect results. Piezoelectric materials are also manufactured in the form of stacks. In a stack configuration multiple layers of identical piezoceramic wafers are stacked on top of one another.

Besides simple shapes such as blocks, plate and beams, various other configurations of piezoelectric actuators as shown in Fig. II. 1 (C-block [18, 49-50], THUNDER [51-52], Moonie [53], Piezoelectric Tube [38-43] and Helicoidal actuator [54-58]) were developed in order to expand the range of output displacement and to meet the requirements of particular applications.

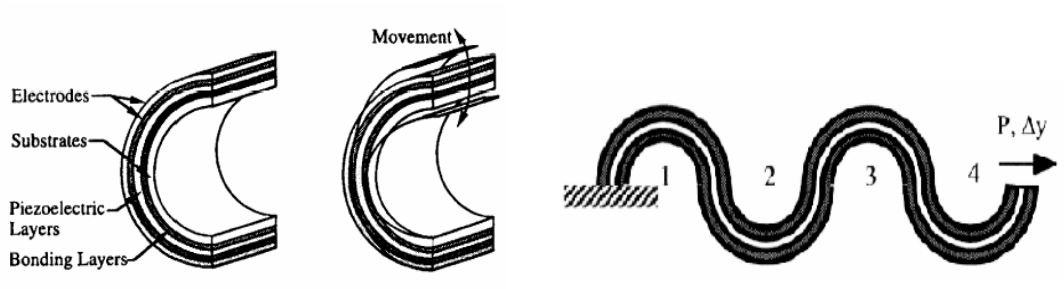

(a) Single and multiple C-block actuator units

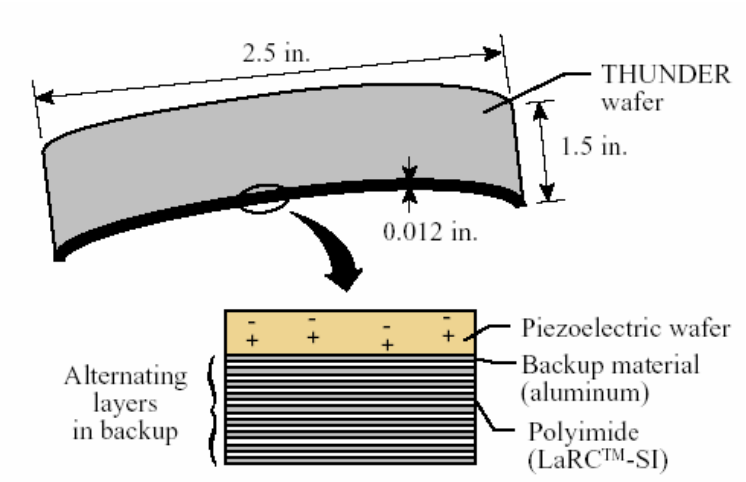

(b) Isometric view of THUNDER wafer and its unrestrained positive actuation

Figure II. 1. Various configurations of piezoceramic actuators

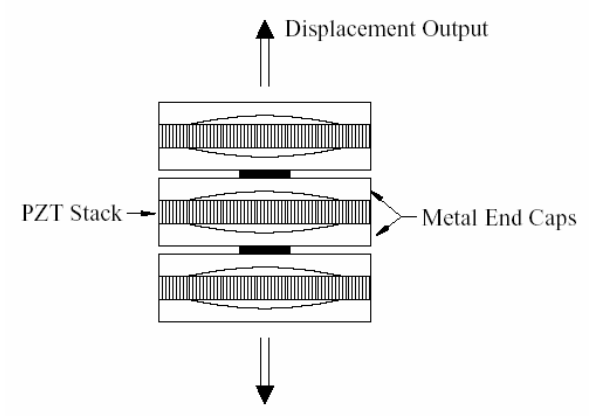

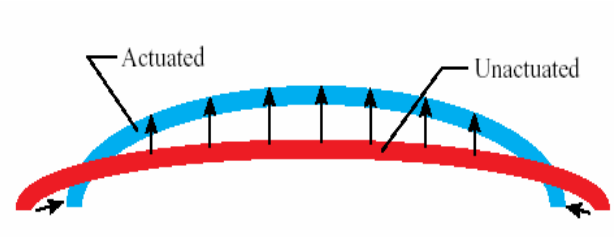

(c) Three Moonie Actuators stacked in Series

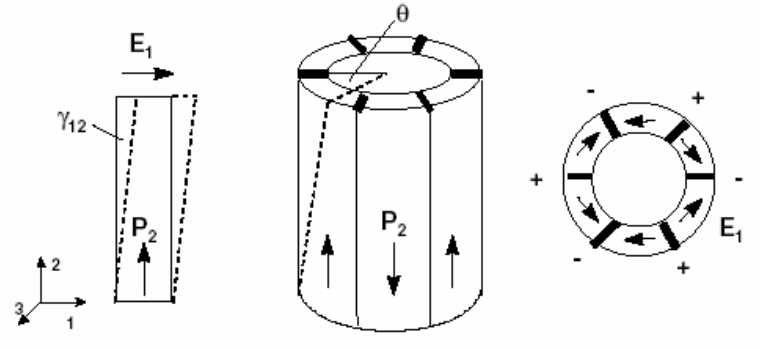

(d) Induced shear piezoelectric tube actuator

Figure II. 1. Various configurations of piezoceramic actuators (continued)

(e) Helicoidal bimorph and PZT implementation

Figure II. 1. Various configurations of piezoceramic actuators (continued)

2.1.1.1 C-BLOCK ACTUATORS

Brei [59] proposed C-blocks which are curved laminate piezoelectric bender actuators as mid-range stiffness actuators. An individual C-block actuator can be stacked in series and/or parallel to increase actuator deflection and/or force. Moskalik and Brei [50] determined the relationship between force and deflection, as well as the free deflection, blocked force, actuator stiffness, and maximum energy transferable to the actuated system. This model also was experimentally verified with three case studies: PZT-5H ceramic unimorphs, PVDF bimorphs, and four-layer bimorphs. The results showed that C-blocks are over six times stiffer, and generate over two-and-a-half times more force than a comparable straight bender. Clement *et. al.* [18] and Clement, Brei, and Barrett [60] developed a C-block actuator for a full-scale active trailing edge flap. Under

low speed wind tunnel testing, the C-block actuator produced a flap deflection of ±8.5°. Further wind tunnel testing was required to validate that large flap deflections are possible at more realistic tip speeds.

2.1.1.2 THUNDER ACTUATORS

THUNDER (THin UNimorph DrivER) actuators are pre-stressed piezoelectric devices developed at NASA Langley Research Center (LaRC) in 1994. THUNDER exhibits large-out-of plane displacements and a very good load carrying capacity relative to other types of piezoelectric actuators. The key factor in the superior performance of THUNDER is the incorporation of a pre-stressing phase during manufacturing. Pinkerton and Moses utilized the THUNDER actuator to alter the upper surface geometry of a subscale airfoil to enhance performance. The results showed that THUNDER can be used to alter the camber of a small airfoil under aerodynamic loads (Jennifer and Robert [61]).

2.1.1.3 MOONIE ACTUATORS

Flextensional actuators typically use a piezoceramic stack and an external amplification mechanism to convert the motion generated by the stack to a usable output motion in the transverse direction. Moonie (Sugawara *et. al.* [53]) is the one of flextensional type actuators. This actuator sandwiches a piezoceramic stack between two end caps having shallow cavities. Displacement of the stack flexes the end caps, producing an increased deflection. The displacement output of the actuator greatly

increases with cavity diameter and depth. Like C-Block actuators, multiple Moonie actuators can be stacked in series (Onitsuka *et. al.* [62]).

2.1.1.4 PIEZOELECTRIC TUBE ACTUATORS

Glazounov and Zhang of the Material Research Laboratory (MRL) at Penn State, and Kim *et. al.* of the Naval Research Laboratory (NRL) initially developed a torsional piezoelectric actuator that transforms piezoelectric shear directly to twist and torque [38-43]. Unlike the bender and stack actuators, the important piezoelectric coefficient in the induced shear strain torsion actuator is d_{15}. The free displacement (twist angle) and blocked torque were developed by an induced shear tube with clamped-free boundary conditions in Ref. 39. One advantage of using induced shear strain in a piezoelectric torsion actuator is that d_{15} piezoelectric coefficient is larger than d_{31} and d_{33}.

2.1.1.5 HELICOIDAL ACTUATORS

Dancila and Armanios [54] proposed and analytically modeled three novel coiled piezoelectric bender actuator. These actuators are capable of producing directly large rotation output without the need for output amplification/conversion mechanisms. An experimental verification was provided by Dancila and Vasilescu [55] for two of the configurations by using actuators manufactured from PVDF.

Pearce, Hooley and Button [56], Pearce, Seffen and Button [57], and Su, Pearce, and Button [58] developed a viscous processing technology that is used for the

manufacture of net-shaped piezoelectric ceramic actuators. Various coiled ceramic actuator configurations have been proposed, manufactured, and tested, including two configurations of coiled bimorph actuators presented by Dancila and Armanios [54], the linear spiral and the helicoidal bimorph. Despite the obvious geometric complexity, the action of pre-coiling, and in a hierarchical manner, offers significantly larger displacements compared to simpler actuators, such as straight rods or bars. This is due to the fact that displacements are generated by the integration of strains along the arc length of the strip. Successive coiling enables a strip of a given length to be packed into a small volume and hence, the magnitude of the output increases relative to the overall size of structure. Seffen [63] showed that the actuated deformations on the original strip are greatly amplified in terms of the displacements output in the overall structure.

Based upon these results it can be concluded that this class of actuators has reached a maturity level at which it is warranted to consider their practical applications, both analytically and experimentally.

2.2 On-Blade Active Systems for Vibration Reduction in Rotorcraft

2.2.1 Active Trailing Edge Flap

Spangler and Hall [12] proposed a piezoelectric bender controlled blade flap. Limited tests were conducted on a nonrotating, nonscaled blade specimen. At the University of Maryland, Barrett [64] used embedded piezoelectric crystals with a closed

loop feedback system to reduce forced flapwise vibrations of a Froude-scaled rotating blade by up to 70%. Additionally, Chen, Samak and Chopra [65] tested a Froude-scaled blade with a trailing edge flap controlled by piezoelectric benders, and achieved 0.2 degree equivalent blade pitch at 6 degree collective and 900 rpm. Clement *et. al.* [18] have demonstrated promising bench top results for a trailing edge flap incorporating C-block actuators. Nitzsche and Breitbach [66] investigated the feasibility of using blade embedded piezoelectric materials to attenuate rotor blade vibrations. Strehlow and Rapp [67] studied the application of smart materials for active control and concluded that a trailing edge flap driven by piezoelectric actuators is feasible. Fabunmi [68] proposed a piezoelectric stack operating in resonance in combination with a ratchet type mechanism to drive a servoflap for rotor control. Ormiston [69] considered a trailing edge flap with embedded smart materials for rotor control. Other concepts proposed for actuating a trailing edge flap include structurally coupled actuators, using bending-torsion (Bernhard and Chopra [14]), extension-torsion (Walz and Chopra [70]) and open section warping-torsion (Giurgiutiu, Rogers, and Mcneil [71]). In conjunction with the development of the above actuation mechanisms there has been significant research on the aeroelastic performance of trailing edge flap rotors and design of advanced adaptive control algorithms (Milgram and Chopra [72]). The Milgram and Chopra study indicates the feasibility of a 10% span, 20% chord trailing edge flap, with ±5º flap travel, in reducing vibratory hub loads.

2.2.2 ACTIVE TWIST BLADE

Bend and Hagood [73] developed the InterDigitated Electrode PiezoFiber Composites (IDE-PFC), shown in Fig. II. 2a. The IDE-PFC system, later renamed Active Fiber Composites (AFC), was embedded within the composite spar of the blade to induce shear stresses which create twist. The AFC actuators are implemented in the form of active plies within the composite spar of the rotor blade. These anisotropic active plies can be oriented at a ± 45 angle to the blade span in order to induce shear stresses and a distributed twisting moment along the blade. In addition, the dense electroceramic active material is positioned around the quarter-chord of the blade section. Figure II. 2 shows a schematic diagram of the integral twist actuation concept as applied to a blade section.

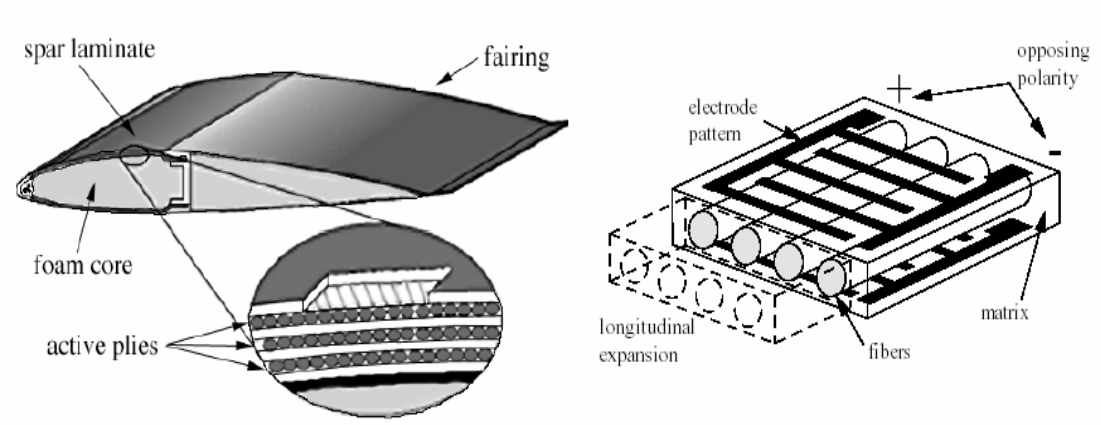

(a) Integral twist actuation concept

(b) Active fiber composite geometry with interdigitated electrode pattern

Figure II. 2. Active Fiber Composite (AFC)

The integral actuation concept eliminates the need for a complex, highly efficient actuation amplification mechanism and does not add any extra profile drag. The primary advantage of the active twist rotor over the trailing edge flap rotor is that it is aerodynamically clean. However, it does require that the actuation forms an integral part of the load path. In order to evaluate the feasibility of the integral twist actuation concept, a modified Rehfield-type single cell composite beam model was developed previously (du Plessis and Hagood [74]).

Interdigitated electrode piezoelectric fiber composite actuators were selected and used in a $1/6^{th}$ scale benchtop twist demonstration. A more advanced rotor dynamic analysis of the integral actuation scheme was later performed (Derham and Hagood [75]). This included a systems-level cost-benefit analysis and demonstrated the potential impact of the integral actuation concept. The design of the integral blade and the development of the actuators, including rigorous structural integrity testing, has been described (Rodgers, Hagood, and Weems [76]). Results from the testing of half-span blade sections and preliminary hover data have also been presented (Rodgers and Hagood [77]).

As applied to rotor blades for the CH-47 helicopter, tests on a 1/16 scaled model blade of that rotorcraft, indicated that twist angles of 1.4° over the blade span were achieved with IDEPFC at 2000 V applied excitation (Derham and Hagood [75]). These result, however, were achieved with a 50% reduction in blade torsional stiffness.

2.2.3 ACTIVE BLADE TIP

An alternative to the above two on-blade actuation systems is to use a segmented rotor blade with active pitching blade tips for vibration control. The attractiveness of the active blade tip concept is that it operates in the blade region with the highest dynamic pressure, and has the potential for effective rotor blade control because the tip has a strong influence on overall rotor performance and loads characteristics. In essence, the active tip is an extension of the free tip and the constant lift rotor concepts.

Stroub [78] developed and investigated analytically a free-tip rotor with a tip that was free to pitch about its own axis, which was located forward of the aerodynamic center. The principle of operation is illustrated by Figure II. 3.

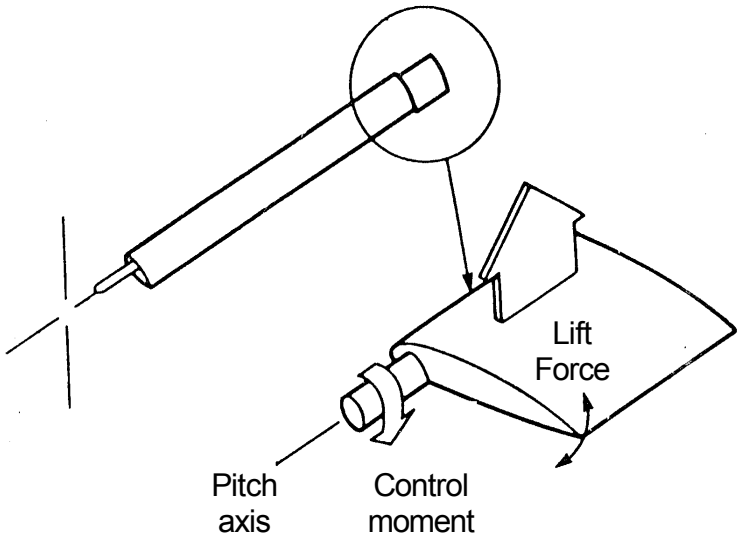

Figure II. 3. Principle operation of free tip

Stroub *et. al.* [79] investigated experimentally a rotor system incorporating a free tip rotor in a wind tunnel test where the free tip extended over the outer 10% of the rotor blade and included a simple, passive controller mechanism. A new tension-torsion strap controller was developed to allow proper evaluation of the free-tip concept. Attractive features of this device were that there was no measurable friction of its own. Test results showed that the free tip rotor reduced power by 12% at an advance ratio of 0.3 and C_T/σ of 0.08, minimized oscillatory flapwise bending moments and oscillatory pitch link loads, and boosted lift by sixteen percent. However, the oscillatory in-plane bending moments were increased. Chopra [80] also analytically demonstrated the aeroelastic benefits of such rotor systems.

Based on the Stroub and Chopra's passive blade tip concept, Bernhard and Chopra [15-16] employed blades with actively pitching blade tip for vibration reduction called a Smart Active Blade Tip (SABT). The tips are actively pitched via a piezo-driven bending-torsion coupled actuator beam that runs down the length of the blade. The experimental test in hover of a one-eighth scale, reduced tip-speed rotor model (tip Mach 0.26), showed that blade tip deflections of the order of 2 deg (half peak-to-peak) were achieved at 2, 3, 4, 5/rev with corresponding dynamic vertical blade root shear variations of the order of 10-20 percent of the nominal blade lift at 8-deg collective ($C_T/\sigma = 0.07$) (Bernhard and Chopra [17]).

2.3 ELASTICALLY TAILORED COMPOSITE STRUCTURE

Over the last decades, the volume and number of applications of composite materials have grown rapidly in the aerospace industry due to their high strength-to-

weight ratio along with significant improvements in fatigue life characterization and damage tolerance assessment. In addition, due to their anisotropic nature, the properties of composites can be easily tailored to incorporate different couplings among elastic modes of deformation within the structure [81-84].

Elastically tailored composite materials provide an extra degree of freedom to meet design requirements efficiently and economically by reducing part counts and weight leading to performance improvement. Two types of elastically tailored composite laminates which have similar configuration but different functions were proposed. Dancila, Kim and Armanios [84] developed and analytically investigated star shape composite structure which have extension-twist coupling, and Kim, Dancila and Armanios [85] experimentally verified the characteristics of the star shape composites. Ha and Dancila [86] proposed a similarly shaped but differently tailored starbeams which are stiff in bending and extension but compliant torsionally. In this study a family of star shape composite laminates is employed to support a helicoidal piezoelectric actuator and a blade tip.

CHAPTER III

A COMBINED PIEZOELECTRIC COMPOSITE ACTUATOR CONFIGURATION AND MODELING

3.1. ACTIVE BLADE TIP CONFIGURATION

A novel combined piezoelectric composite actuator configuration is proposed and analytically modeled in this work. The actuator is a low complexity, active compliant mechanism obtained by coupling a modified star cross sectional configuration composite beam with a helicoidal bimorph piezoelectric actuator coiled around it (Fig. III. 1). The modified star beam is tailored and optimized to achieve increased torsional compliance and bending stiffness at given constant axial stiffness. The coiled piezoelectric actuator is designed to directly generate finite rotation output without the need for mechanisms to amplify the piezoelectric displacement output and/or convert linear output to rotational output.

The proposed cylindrical actuator configuration is compact and is a good candidate for use as a hinge tension-torsion bar actuator for a helicopter rotor blade flap or blade tip (Fig. III. 2). For such cases the modified star composite beam also carries the centrifugal loads of the flap or blade tip, and those of the coiled actuator, thereby eliminating the need for a thrust bearing. Consequently, friction/sticktion and backlash

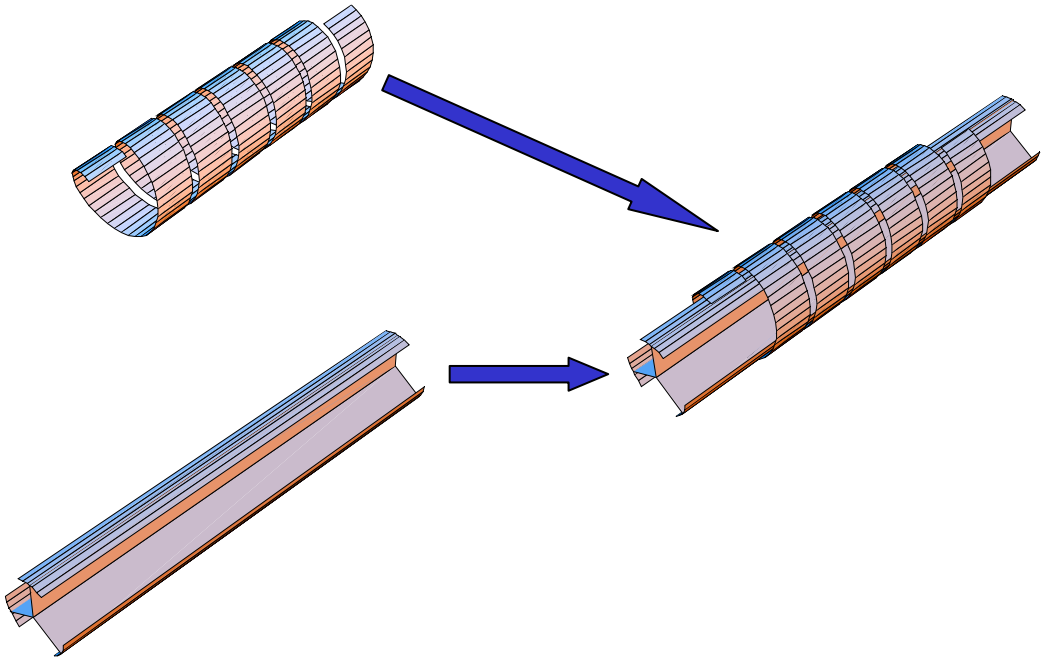

Figure III. 1. A combined piezoelectric-composite actuator configuration

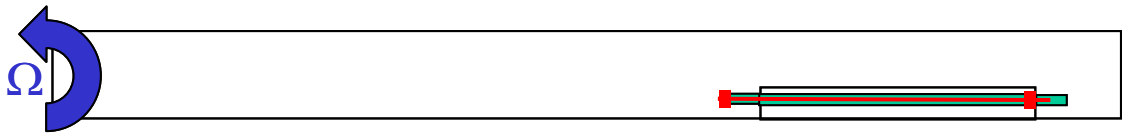

(a) Active flap application

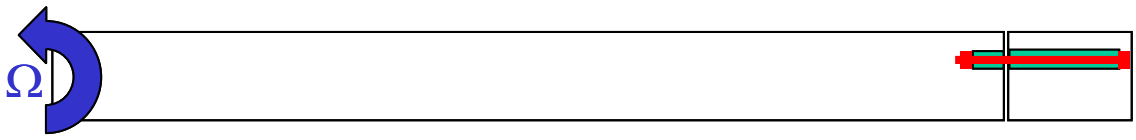

(b) Active blade tip application

Figure III. 2. Applications of a combined piezoelectric-composite actuator as tension-torsion hinge bar actuator

effect that represent difficulties commonly encountered by other induced strain blade actuation configurations are eliminated.

Prior conceptual and modeling work on coiled piezoelectric actuators and modified star composite beam, two technologies forming the basis for the actuation concept proposed and modeled in this work, are briefly outlined in this chapter.

3.1.1. A REVIEW OF COILED BENDER PIEZOELECTRIC ACTUATORS

Piezoelectric actuators have been designed for applications such as precision tooling, adaptive optics, vibration suppression, helicopter rotor blade control, and adaptive structures. Although piezoelectric actuators are capable of producing high forces with accuracy, they are generally limited in terms of their output displacement capability. For example, a typical piezoelectric ceramic stack actuator can produce a maximum strain of approximately 0.1%. There is a need to extend this technology to handle large forces as well as large displacements, especially for shape control applications.

Because the output motion of piezoelectric actuators is limited to very small displacements, various application schemes have been developed to improve the output stroke performance. As would be expected, mechanical linkage are often employed. However, using mechanical linkages as amplification devices can severely limit the overall effectiveness of the actuator due to clearances in the mechanical joints. Joint clearances are significant when compared to the total stroke of the actuator material which is in the micron range, and may render the entire actuator ineffective. Besides the

clearance of joints and mechanical complexity of the linkage assembly, mechanical conversion from linear output to rotational output also causes a loss of efficiency.

Recently, coiled bender piezoelectric actuators have been proposed, modeled and experimentally validated independently by Dancila and Armanios [54], and Dancila and Vasilescu [55], at Georgia Tech, and by Pearce, Seffen, and Button [57] at the University of Birmingham in the UK based upon a net shape manufacturing technology using a proprietary viscous processing (Su, Pearce, and Button [58]). These actuators are capable of finite rotation output without the need for mechanisms of displacement amplification and/or conversion of linear to rotational output [87].

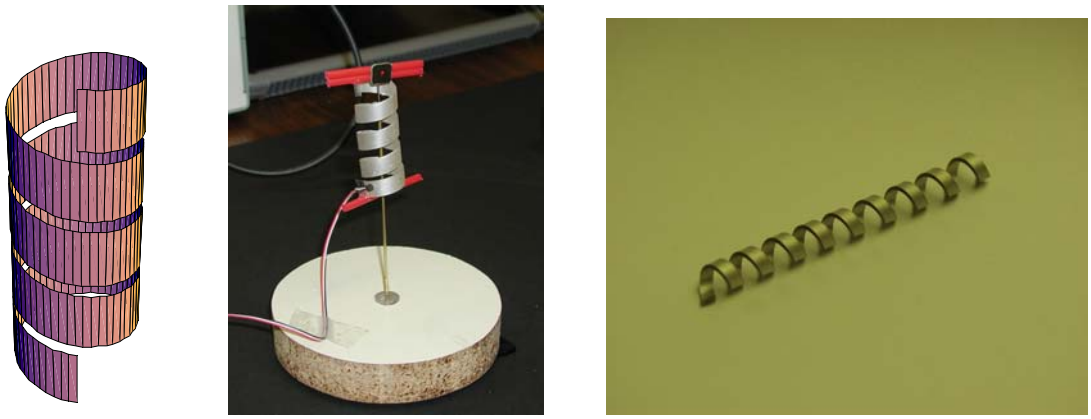

(a) (b) (c)

Figure III. 3. Helicoidal bimorph piezoelectric actuators

(a) Helicoidal Bimorph, (b) PVDF Implementation, and (c) PZT Implementation

Courtesy T. Button University of Birmingham, UK

One of the three configurations proposed in Ref. 54, the helicoidal bender is shown in Fig. III. 3a, with implementations using PVDF (Dancila and Armanios [55]) and PZT (Pearce, Seffen, and Button [57]) shown in Fig. III. 3b and 3c, respectively.

3.1.2. CONCEPT OF A MODIFIED STAR SHAPE BEAMS

Straub *et. al.* [31] have investigated an active helicopter blade flap concept using piezoelectric stack actuators with an X-frame displacement output amplification. In order to eliminate the friction caused by the centrifugal loading on the flap, Ref. 31 makes use of a tension-torsion bar to create a compliant mechanism for supporting the flap. The tension-torsion bar is cantilevered into the blade at the proximal flap end, and is cantilevered into the flap at its distal end, thus carrying the flap centrifugal force directly as a tensile load and eliminating the need for a thrust bearing. The tension-torsion bar extended beyond the distal flap end and into the blade, being supported in a cylindrical joint. The tension-torsion bar used consisted of a circular cylindrical steel rod of small diameter. Its low bending rigidities required the use of several additional intermediate cylindrical joint supports spaced over the length of the flap. Pitch deflections of the flap are made possible by the twisting of the tension-torsion bar. Consequently, in order to reduce the actuation effort, the torsional rigidity of the tension-torsion bar needs to be low. In order to eliminate the need for intermediate supports the bending rigidity of the tension-torsion bar should be high.

The solution of Ref. 31 can be also used for a helicopter blade tip in order to eliminate the need for a thrust bearing and to allow friction/sticktion free pitching. The

tension-torsion bar should be cantilevered into the blade at the proximal blade tip end and into the blade tip at the distal end. Again, in order to reduce the actuation effort the torsional stiffness of the tension-torsion bar should be low. Since the blade tip is subject to airloads and the option of using intermediate cylindrical supports does not exist, the bending rigidity of the tension-torsion bar needs to be high.

Consequently, a tension-torsion bar used as a compliant mechanism for the support of either a helicopter blade tip or that of a helicopter blade flap needs to satisfy the following requirements: i) high axial stiffness and strength; ii) high bending stiffness; and iii) low torsional stiffness.

Modified star beam cross sectional composite beams have been proposed and modeled by Ha and Dancila [86] at Georgia Tech. This cross sectional configuration was developed from the star beam configuration, which was developed by Dancila, Kim, and Armanios [84] for composite beams with extension twists coupling, as a means of increasing the cross sectional bending stiffness from the case of a strip without sacrificing their high level of extension twist coupling [84-85].

3.2. MODELING APPROACH

A detailed analysis for compact bimorph actuators, linear spiral, helicoidal, and hybrid geometric configurations can be found in Ref. 54. A simple analytical model for a helicoidal bimorph actuator will be reviewed and overall torsional stiffness and blocked actuator moment will be also discussed.

In this work an extension of the star configuration, the modified star configuration, is proposed and analyzed. A simple analytical model is developed based upon the thin

walled beam theory and is applicable when the thickness of the strip is much smaller that the width, and for isotropic materials or composite materials with 0 degrees or 90 degrees lay-up. A finite element modeling using the commercially available code ABAQUS [88] and the research cross sectional analysis code SVBT, developed by Bauchau at Georgia Tech, are used to numerically model the response. The analytical model developed, shown to be accurate enough, is subsequently used for a trend analysis.

The applicability and effectiveness of a combined piezoelectric-composite actuator to the problem of pitching control of an active rotor blade tip in the presence of incompressible flow airloads are investigated in the work. An analytical model for the piezoelectrically actuated blade tip will be developed and used to analyze and identify the effect of inertial and aerodynamic forces on blade tip response. The sensitivity of amplified blade tip response as function of hinge position will be also investigated in order to use the benefit of aerodynamic loading.

Flexible multi-body dynamics code DYMORE [89], developed by Bauchau at Gerogia Tech., will be used to numerically find the response of the blade/wing tip and compare it with analytical results.

3.3 CHARACTERIZATION OF A COILED BENDER PIEZOELECTRIC ACTUATOR

A detailed analysis for compact bimorph actuators, linear spiral, helicoidal, and hybrid geometric configurations can be found in Ref. 54 and 87.

For a coiled bender actuator shown in Fig. III. 4, a geometric definition of the actuator midplane geometry is given, in a polar coordinate system, by Eq. (1), where

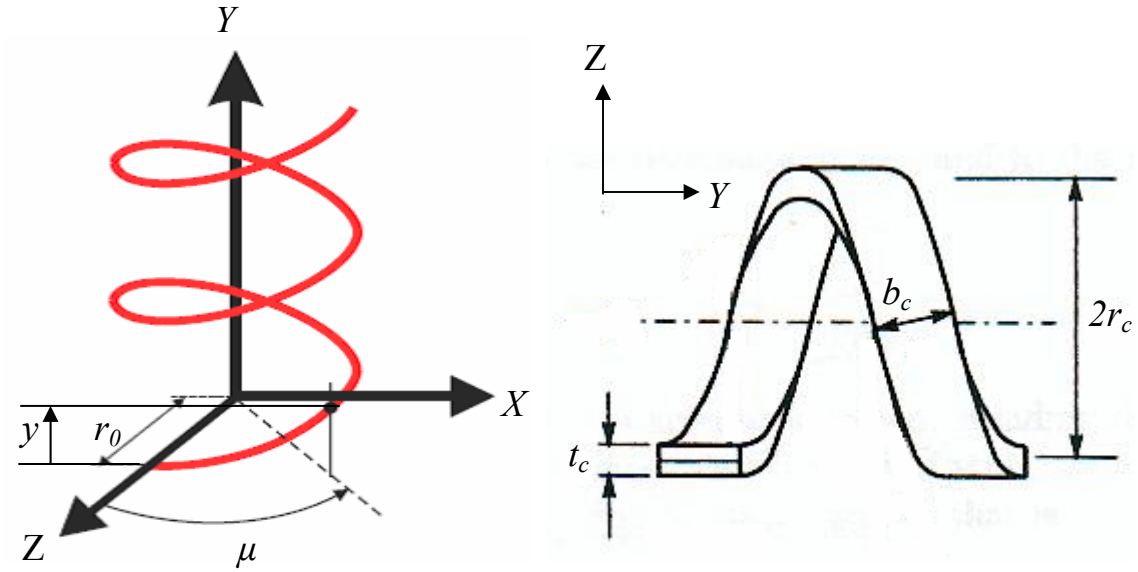

(a) Initial midplane geometry of a coiled bender actuator

(b) Single turn of a coiled bender actuator and geometry

Figure III. 4. Geometry of a coiled bender actuator

μ is the current coil angle, Σ is the total coil wrapping angle, κ_1 is the radial increment, b_c is the coil width measured in the axial y direction, and r_0 is the coil midplane radius:

$$r_c(\mu, y) = r_0 \qquad \begin{matrix} 0 \le \mu \le \Sigma \\ \kappa_1 \mu \le y \le \kappa_1 \mu + b_c \end{matrix} \tag{1}$$

and where the additional condition

$$2\pi\kappa_1 > b_c \tag{2}$$

should be satisfied to prevent coil overlapping. The length of the coil midline is given by

$$L_c = \sum \sqrt{\left(r_0^2 + \kappa_1^2\right)} \tag{3}$$

Assuming that the condition $t_c \square r_c$ is satisfied, where t_c is the bimorph coil thickness, the change in principal curvature of the shell surface with applied electric field intensity, E_3, can be computed as

$$k_c = \frac{3 d_{31} E_3}{t_c} \tag{4}$$

where d_{31} is the 3-1 piezoelectric strain component and E_3 the applied 3-direction electric field and the cross-sectional blocked moment by using

$$M_c(V) = \frac{E_c d_{31} E_3 t_c{}^2 b_c}{4} = \frac{E_c d_{31} t_c b_c}{4} V \tag{5}$$

and where E_c is the constant electric field 1-1 elastic stiffness constant of the coiled actuator, V is the applied voltage. The electric field intensity $E_3=V/t_c$ is determined by the control voltage applied and is restricted to the maximum value of E_d to prevent the depolarization of the piezoelectric material.

Assuming one end of the coil to be fixed, the free rotation angle of the opposite actuator end can again be obtained by integration of incremental cross-sectional rotation angles, θ_c, along the entire coil length

$$\theta_c = \int_0^{L_c} k_c \frac{r_0 ds}{\sqrt{\left(r_0^2 + \kappa_1^2\right)}} = k_c r_0 \sum \tag{6}$$

The blocked moment is then expressed by the rotation angle of the coiled actuator.

$$M_c(V) = \left(EI\right)_c k_c = \left(\frac{E_c t_c^{\,3} b_c}{12} \frac{1}{\sum r_0}\right) \theta_c = K_{coil} \theta_c \tag{7}$$

where K_{coil} is the overall torsional stiffness of the coiled actuator.

The beneficial characteristics of this actuator configuration are revealed by Eqns. (5-7). The blocked moment in Eq. (5) does not depend upon the length of the actuator, while the free rotation angle, Eq. (6) does increase with actuator length. Equation (7) shows that the overall torsional stiffness is also reduced inversely proportional to actuator length.

3.4. MODELING OF A MODIFIED STAR SHAPE CROSS-SECTIONAL BEAM

3.4.1. GEOMETRIC CONFIGURATION AND RIGIDITIES

Star shaped and modified star shaped cross sectional configurations are shown in Fig. III. 5 and Fig. III. 6, respectively.

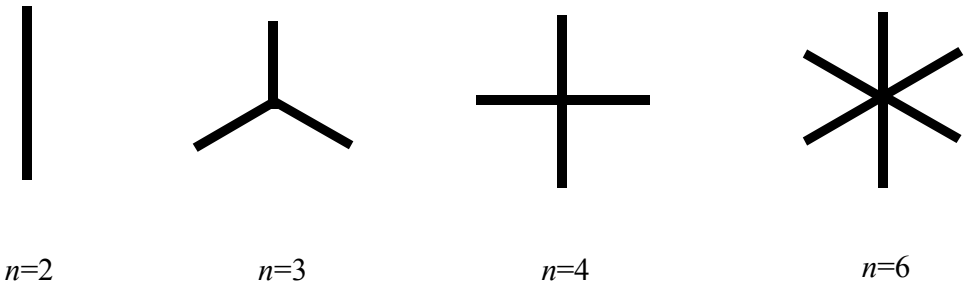

Figure III. 5. Star shape cross sectional configurations

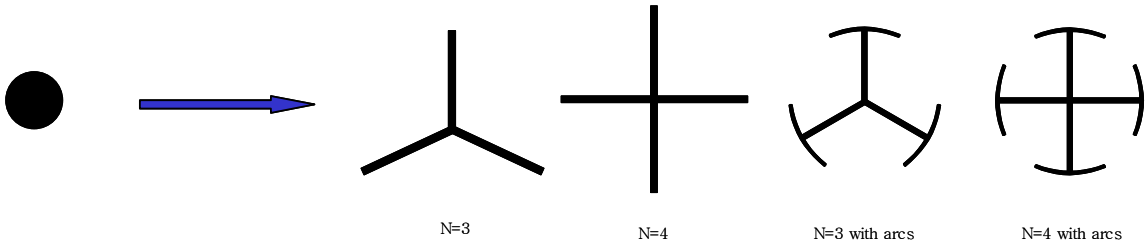

Figure III. 6. Redistribution of a circular cross sectional area (star shape and modified star shape configurations)

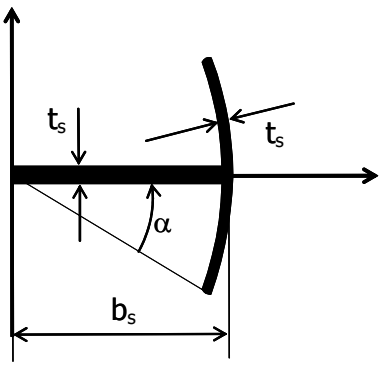

Figure III. 7. A geometric configuration of a modified starbeam

Figure III. 7 shows one arm of a modified star configuration, where t_s denotes the thickness of the wall, b_s represents the radius of the star cross section and α represents the side angle of the extension arc. If $\frac{t_s}{b_s} << 1$, a simple analytical model can be developed based upon a thin walled beam approximation. Introducing the nondimensional parameters, $\varphi = \frac{N_s \alpha}{\pi}$, with $0 \le \varphi \le 1$, and $\eta = \frac{t_s}{b_s}$, with $\eta \le 0.1$, the case of $\varphi = 0$ corresponds to star configurations and the case $\varphi > 0$ corresponds to modified star configurations.

Due to symmetry, the centroid of the modified star cross section is always a principal point, which means that the second moment of area with respect to any axis passing through the centroid is a constant. Therefore, a single value is sufficient to characterize the bending stiffness of the cross section.

It can be shown that the axial stiffness of the modified star beam is given by

$$(EA)_s = E_s N_s b_s^2 \eta \left(1 + \frac{2\pi\varphi}{N_s}\right) \tag{8}$$

that the bending stiffness is given by

$$(EI)_s = E_s \frac{N_s}{2} b_s^4 \eta \left(\frac{1}{3} + \frac{2\pi\varphi}{N_s} + \frac{\eta^2}{12}\right) \tag{9}$$

and that the torsional stiffness is given by

$$(GJ)_s = G_s \frac{N_s}{3} b_s^4 \eta^3 \left(1 + \frac{2\pi\varphi}{N_s}\right) \tag{10}$$

An ABAQUS finite element model of a modified star beam, shown in Fig. III. 8, has been developed.

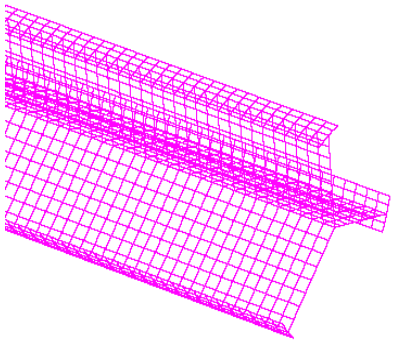

Figure III. 8. ABAQUS FEM model of a modified starbeam

The model consists of 97,200 reduced integration shell elements of type S4R, with a side aspect ratio of 1:2 at the most. This model allows for both isotropic and anisotropic (composite) material properties. Beam cross sectional stiffnesses have been determined indirectly by using the relative displacement of cross sections located at 25% and 75% along the beam, respectively, in response to appropriate loading conditions. The specified cross sections have been selected in order to eliminate any significant influences of end effects.

A cross sectional SVBT finite element model, shown in Fig. III. 9, has been developed. It consists of 1104 4-noded elements with side aspect ratio of 1:5 at the most. This model also allows for both isotropic and anisotropic (composite) material properties. Beam cross sectional stiffnesses have been determined directly by using this model.

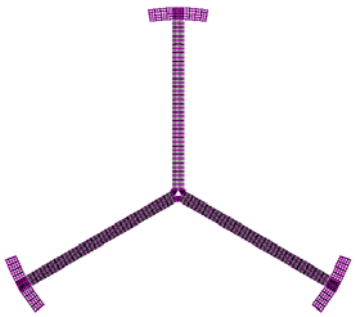

Figure III. 9. SVBT cross sectional FE model

3.4.2. COMPARISON OF MODEL PREDICTIONS

Assuming composite material with the experimentally determined properties shown in Table III. 1 (Kim [90]) and a unidirectional lay-up of 0 degrees, a comparison of cross sectional stiffness predictions among the three models has been performed. The geometric characteristics shown in Table III. 2 have been used, and the results of the comparison are shown in Table III. 3.

Table III. 1. Material Properties

Material Properties (Hexcel IM7/8551-7 Gr/Ep)	
Parameters	Value
E_{11}	142.6 GPa
E_{22}	8.39 GPa
$G_{12}=G_{13}$	3.9 GPa
G_{23}	3.3 GPa
$\nu_{12}=\nu_{13}$	0.34
Number of plies	8
Ply thickness	0.156 mm

Table III. 2. Geometric Characteristics

Geometric Properties	
Parameters	Value
Width	20 mm
Thickness	8x0.156 mm
Length	2 m
Arc Angle	0.16 rad
Number of strips	3

Table III. 3. Comparison of Predictions

		Analytical	ABAQUS		SVBT	
Starbeam	$E_{11}A$	1.0678E+07	1.06783E+07	0.00371%	1.05221E+07	1.46%
	$E_{11}I$	7.1255E+02	7.09713E+02	0.4%	7.11534E+02	0.14%
	$G_{12}J$	1.5161E-01	1.49343E-01	1.50%	1.49527E-01	1.37%
Modified Starbeam	$E_{11}A$	1.4095E+07	1.40592E+07	-0.25%	1.40444e+07	0.36%
	$E_{11}I$	1.3959E+03	1.38546E+03	-0.75%	1.46043e+03	4.62%
	$G_{12}J$	2.0013E-01	2.05440E-01	2.65%	2.05096e-01	2.48%

It can be seen from Table III. 3 that a very good general agreement among the three sets of predictions is obtained. Using the analytical predictions as reference, the SVBT-predicted stiffnesses show the largest percentage variation of less than 5%. While it is expected that the SVBT prediction set is the most accurate, it can nevertheless be concluded that the predictions of the analytical model are accurate enough to be used in the following for a trend analysis with regards to the effects of the non dimensional cross sectional parameters N_s, φ and η.

Defining the diameter of the same-area circular cross section as

$$d = \sqrt{\frac{4N_s b_s^{\,2}\eta}{\pi}\left(1+\frac{2\pi\varphi}{N_s}\right)} \tag{11}$$

and using the stiffnesses of this circular cross section as reference, the ratio of the axial, bending and torsional stiffnesses for the modified star beam are given by

$$\frac{(EA)_s}{(EA)_{circular}} = 1 \tag{12}$$

$$\frac{(EI)_s}{(EI)_{circular}} = \frac{2\pi}{N_s \eta} \frac{\left(\frac{2\pi\varphi}{N_s} + \frac{\eta^2}{12} + \frac{1}{3} \right)}{\left(1 + \frac{4\pi\varphi}{N_s} + \frac{4\pi^2\varphi^2}{N_s{}^2} \right)} \tag{13}$$

$$\frac{(GJ)_s}{(GJ)_{circular}} = \frac{2\pi\eta}{3N_s} \frac{\left(\frac{2\pi\varphi}{N_s} + 1 \right)}{\left(1 + \frac{4\pi\varphi}{N_s} + \frac{4\pi^2\varphi^2}{N_s{}^2} \right)} \tag{14}$$

For the limit case of $\varphi = 0$ (star beam case), these expression reduce to

$$\frac{(EA)_s}{(EA)_{circular}} = 1 \tag{15}$$

$$\frac{(EI)_s}{(EI)_{circular}} = \frac{\pi}{6N_s \eta} \left(\eta^2 + 4 \right) \tag{16}$$

$$\frac{(GJ)_s}{(GJ)_{circular}} = \frac{2\pi\eta}{3N_s} \tag{17}$$

The variation of *GJ* and *EI* ratios as a function of φ for $\eta = 0.1$ and $N_s = 3, 4, 5, 6$ are shown in Fig. III. 10 and Fig. III. 11, respectively. It is immediately apparent that the redistribution of the cross sectional material from a circular configuration to a star or modified star configuration shown in Fig. III. 6 has great benefits for a tension-torsion bar application. For the parameter choice shown the torsional stiffness can be reduced to less than 7% while the bending stiffness can be increased more than seven fold and the axial stiffness is preserved.

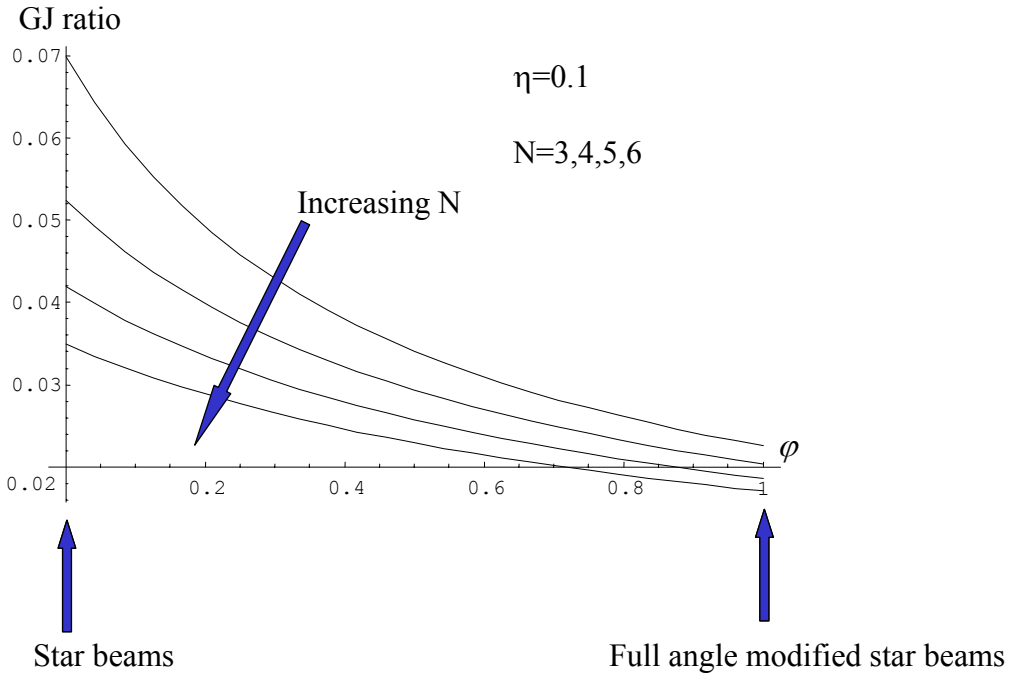

Figure III. 10. Variation of *GJ* ratio

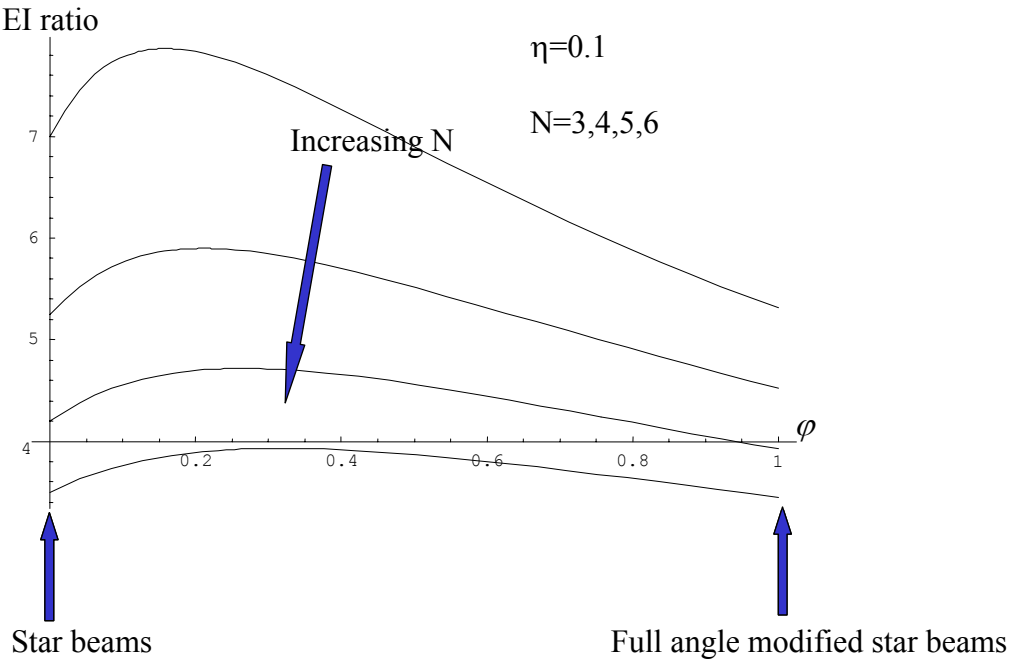

Figure III. 11. Variation of *EI* ratio

It can be also observed that the bending stiffness ratio has a maximum point for some non zero value of φ. This proves that for tension-torsion applications a modified star represents an improvement over a star configuration, since as φ increases from 0 both stiffness ratios show a beneficial trend: *GJ* decreases while *EI* increases. To determine this optimum configuration we use

$$\frac{\partial(EI)}{\partial\varphi} = 0 \tag{18}$$

to obtain

$$\varphi_{opt} = \frac{N_s(2-\eta^2)}{12\pi} \approx \frac{N_s}{6\pi} \tag{19}$$

The variation of *EI* ratio and the corresponding values of φ_{opt} for $N_s = 3$ and 4, respectively, are shown in Fig. III. 12 and Fig. III. 13.

A surface plot of the variation of *GJ* and *EI* ratios with both φ and η over the range of values of interest is shown in Fig. III. 14 and Fig. III. 15, respectively.

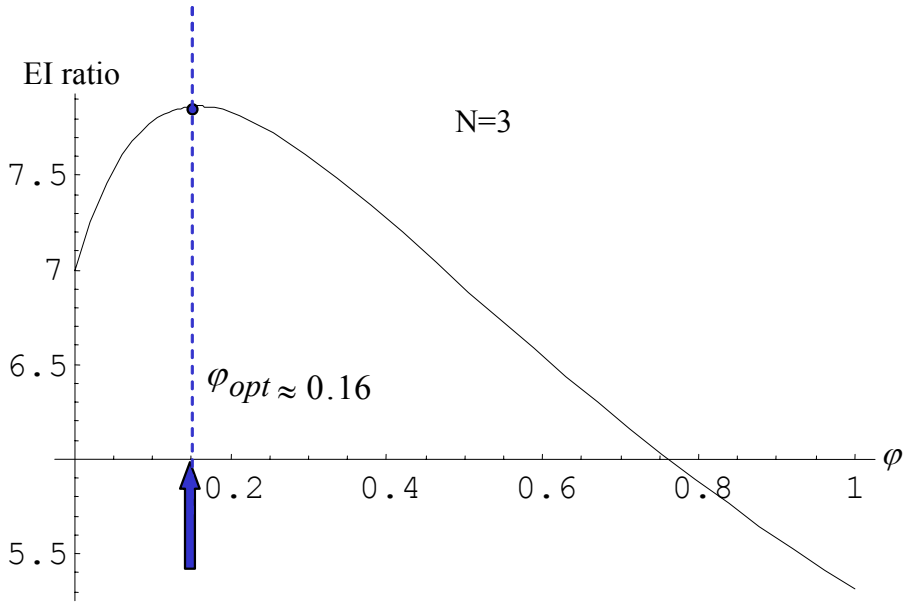

Figure III. 12. Optimal *EI* ratio for *N*=3

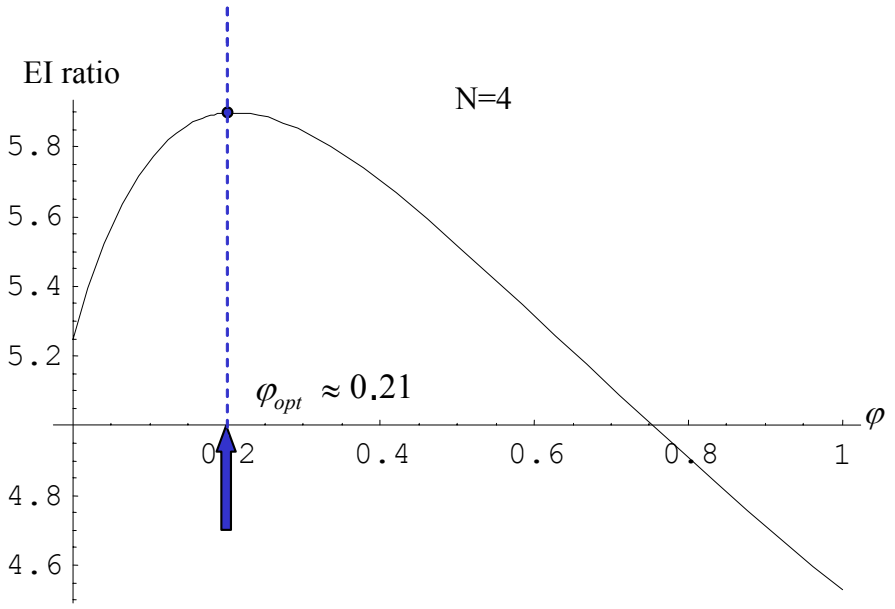

Figure III. 13. Optimal *EI* ratio for *N*=4

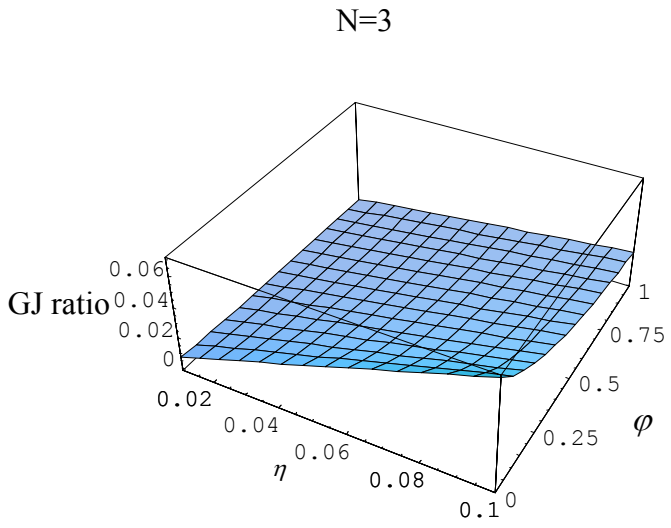

Figure III. 14. Surface plot of *GJ* ratio variation for *N*=3

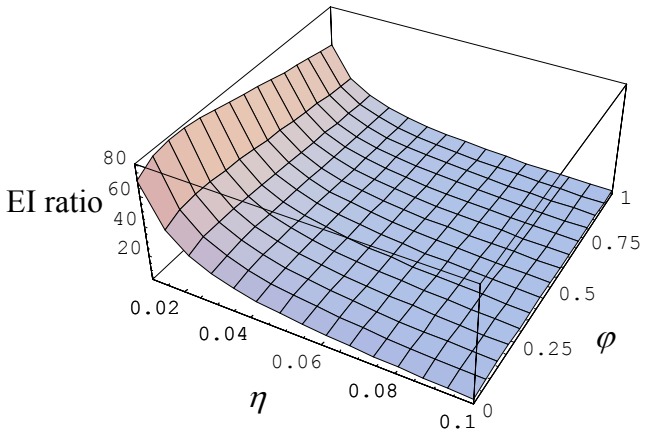

Figure III. 15. Surface plot of *EI* ratio variation for *N*=3

Finally, the variation of *GJ* and *EI* ratios with N_s for $\eta = 0.05$ and $\varphi = \varphi_{opt}$ is shown in Fig. III. 16 and Fig. III. 17, respectively.

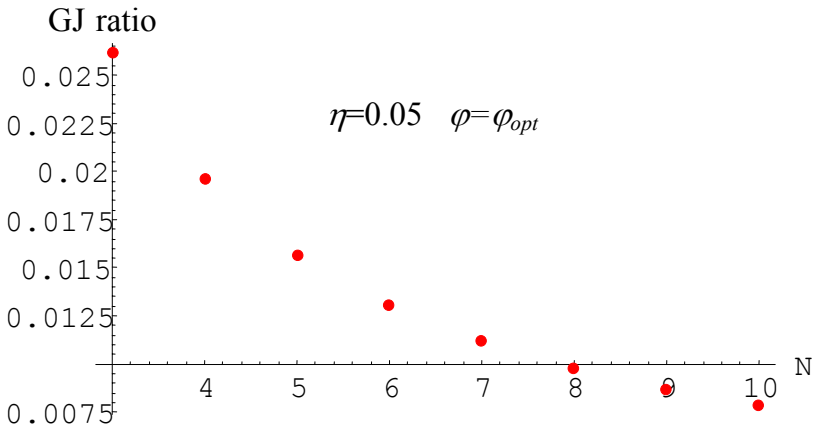

Figure III. 16. Variation of *GJ* ratio with *N*

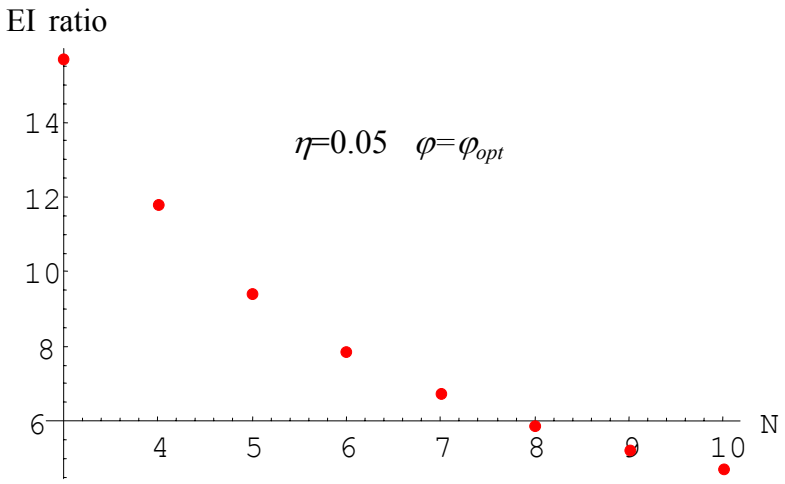

Figure III. 17. Variation of *EI* ratio with *N*

3.4.3. CHARACTERIZATION OF A MODIFIED STARBEAM

Based on the previous parametric studies about geometry and stiffness, the behavior of the modified starbeam subjected to either axial force or tip torque is calculated and the tip twist angle of the modified starbeam subjected to both axial force and tip torque is determined.

Consider the idealized problem of an infinitely long modified starbeam with constant cross sectional area so that boundary effects can be negligible, as depicted in Fig. III. 18.

(a) Axial load

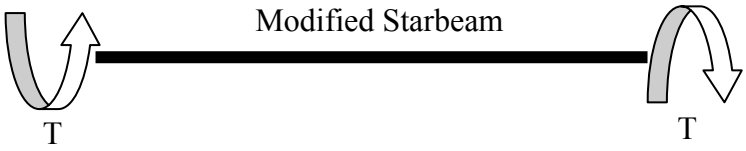

(b) Tip torque

(c) Combined axial load and torque

Figure III. 18. A modified starbeam subjected to several types of loading

First, consider a modified starbeam subjected to constant axial load, F, applied at the tip of the beam depicted in Fig. III. 18(a). Because cross sectional area is constant, the axial force F_y is simply obtained by introducing the normal stress distribution to find

$$F_y = \int_{Area} \sigma_y dA = \int_{Area} E_s \varepsilon_y dA = (EA)_s \, \varepsilon_y = F$$
$$\varepsilon_y = \frac{dU_y}{dy} = Const. \tag{20}$$

where σ_y is the normal stress and ε_y is the axial strain.

Second, consider a modified starbeam subjected to tip torques, T, of equal magnitude and opposite directions depicted in Fig. III. 18(b). Assuming uniform torsion along the axis of the beam, the torque acting on the cross section along the axis of the modified starbeam is obtained by

$$\begin{aligned} T_y &= (GJ)_s \phi_s = T \\ \phi_s &= \frac{d\theta_s}{dy} = Const. \end{aligned} \tag{21}$$

where $(GJ)_s$ is the torsional stiffness and ϕ_s is the twist rate of the beam.

Finally, consider the modified starbeam subjected to combined constant axial loads and torques applied at the end tips of the beam as shown in Fig. III. 18(c). The governing equation exhibiting the apparent torsional stiffening of the modified beam is expressed by Eq. (22). Details of the derivation of Eq. (22) are presented in Appendix A.

$$T = \left[(GJ)_s + \frac{FI_s}{A_s} \right] \phi_s + E_s I_{NL} \phi_s^3 \tag{22}$$

where $\phi_s \left(= \frac{d\theta_s}{dy} \right)$ is twist rate, I_s is the second moment of area and I_{NL} is the nonlinear term related to the moment of area of the modified starbeam.

The applied tip torque can be represented in terms of the tip twist angle, θ_s

$$T = \left[\frac{(GJ)_s}{L_S} + \frac{FI_s}{A_s L_s} \right] \theta_s + \frac{E_s I_{NL}}{L_s^3} \theta_s^3 = \left(K_{el} + K_F \right) \theta_s + K_{NL} \theta_s^3 \qquad (23)$$

where K_{el}, K_F, and K_{NL} represent the elastic torsional stiffness, the apparent torsional stiffness due to axial load and the nonlinear term identified as due to trapeze effect.

3.5. CHARACTERIZATION OF A COMBINED PIEZOELECTRIC-COMPOSITE ACTUATOR

A combined piezoelectric-composite actuator can be obtained by loosely coiling a helicoidal bender around a modified star beam (Fig. III. 19) and connecting the two components through a set of pinned points, such that subject to axial loads the piezoelectric actuator load is transferred to the modified star beam.

Considering the combined piezoelectric-composite actuator subjected to axial load, *F*, applied at the tip and tip torque, *T*, only from a coiled actuator shown in Fig. III. 19, the moment equilibrium equation at the tip is given by:

$$T = M_c(V) = \left[K_{coil} + K_{el} + K_F(F) \right] \theta + K_{NL} \theta^3 \qquad (24)$$

where,

$$M_c(V) = \frac{E_c d_{31} t_c b_c}{4} V \qquad (25)$$

$$K_{coil} = \frac{E_c t_c^3 b_c}{12} \frac{1}{\sum r_0}, \; K_{el} = G_s \frac{N_s}{3L_s} b_s^4 \eta^3 \left(1 + \frac{2\pi\varphi}{N_s} \right), \; K_F = \frac{FI_s}{A_s L_s}, \; K_{NL} = \frac{E_s I_{NL}}{L_s^3}$$

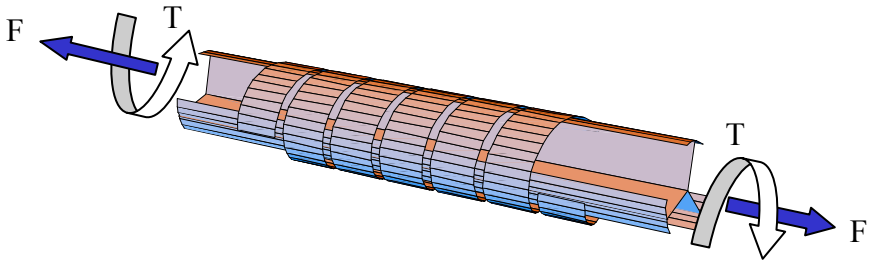

Figure III. 19. A modified starbeam subjected to combined loading

The tip twist angle of the combined actuator is expressed in terms of the axial load, F, and applied voltage, V

$$\theta(F,V) = \frac{-2^{1/3}\left(K_F(F) + K_{coil} + K_{el}\right)}{\left[27M_c(V)K_{NL}{}^2 + \sqrt{108\left[K_F(F) + K_{coil} + K_{el}\right]^3 K_{NL}{}^3 + 729M_c(V)^2 K_{NL}{}^4}\right]^{1/3}}$$

$$+ \frac{\left[27M_c(V)K_{NL}{}^2 + \sqrt{108\left[K_F(F) + K_{coil} + K_{el}\right]^3 K_{NL}{}^3 + 729M_c(V)^2 K_{NL}{}^4}\right]^{1/3}}{3\times 2^{1/3} K_{NL}} \quad (26)$$

Neglecting the nonlinear term, K_{NL}, an approximate tip twist angle is simply given by

$$\theta_{approx}\left(F,V\right)=\frac{M_c\left(V\right)}{\left[K_F\left(F\right)+K_{coil}+K_{el}\right]} \tag{27}$$

Assuming no axial loading, the tip twist angle is obtained by

$$\theta\left(V\right)=\frac{M_c\left(V\right)}{\left(K_{coil}+K_{el}\right)} \tag{28}$$

which is smaller than the value for the helicoidal coil alone (Fig. III. 20). The effects of the axial load and control voltage applied on the tip twist angle of the combined actuator are shown in Fig. III. 21. The used geometric properties of combined piezoelectric composite actuator are shown in Table III. 4.

Table III. 4. Geometric Properties of Combined Piezoelectric Composite Actuator

Modified starbeam	Value	Coiled bender acuator	Value
Number of plies	4	Total coil angle (Σ)	61.475 rad
Ply thickness (t_s)	0.156 mm	Thickness (t_c)	0.0003 m
Number of strips (N_s)	4	Width (b_c)	0.0346 m
Arc angle (α)	0.21 rad	Midplane radius (r_c)	0.0035 m
Length (L_s)	0.5 m	Geometric parameter (κ_1)	1.3

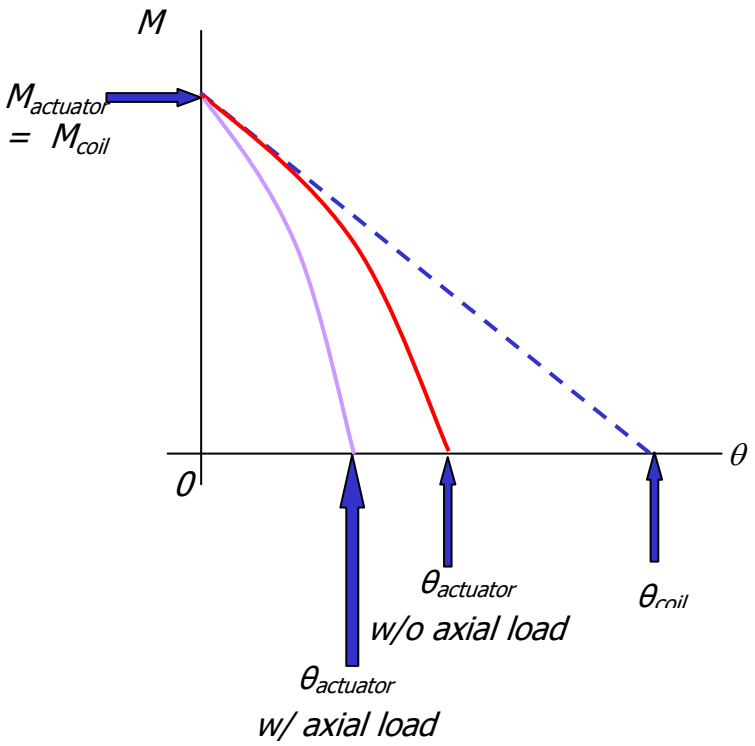

Figure III. 20. Free rotational angle of a combined actuator

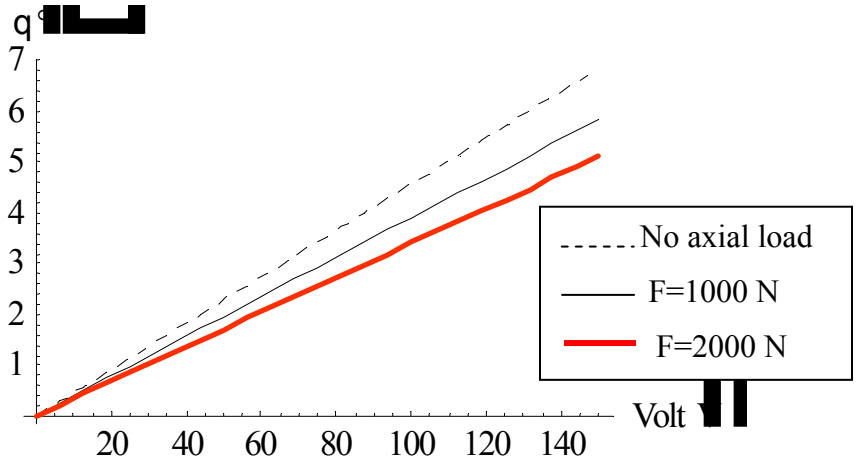

Figure III. 21. Effects of applied voltage and axial load on the tip angle of a combined actuator

CHAPTER IV

APPLICATION OF A COMBINED PIEZOELECTRIC-COMPOSITE ACTUATOR TO WING/BLADE TIPS

This chapter analyzes the applicability of the combined piezoelectric-composite actuator to a helicopter blade tip and to a wing tip to control lift and vibrations. The aerodynamic loading and centrifugal effect applied on the blade tip is first described, and then equilibrium equations at the blade tip are established. To analyze the aerodynamic effects over the coupled actuator and blade tip, the wing tip is considered with a chosen combined actuator configuration.

4.1 AERODYNAMIC LOADING

The airload distribution created over the active blade tip deflected at an angle of attack independent of the main blade pitch angle is established through aerodynamic modeling. The aerodynamic model used is based on the 2D quasi-steady linear aerodynamics related to a non-uniform inflow evaluated by the blade element momentum theory [91].

Using this approach, the local lift is evaluated independently and expressed by an analytical variation of collective pitch angle, β, and the deflection angle of active blade tip, θ.

The analytical expression of the total lift loading over the active blade tip is estimated in Eq. (29) by integrating the local blade lift coefficient, given as a function of collective pitch angle, deflected blade tip angle and Mach tip number,

$$L_{aero}\left(\beta,\theta,M_{Tip}\right)=\frac{1}{2}\rho a^2 M_{Tip}^2 cR\int_{(1-E)}^{1} C_l^{\alpha}\left(\beta+\theta-\frac{\lambda(r)}{r}\right)r^2 dr \tag{29}$$

where *E* is defined as the ratio between blade tip span and blade radius.

The non-uniform inflow, λ, is modeled as function of local angle, $\beta+\theta$, being parametrically dependent of rotor solidity, σ.

$$\lambda=\frac{\sigma C_l^{\alpha}}{16F(\lambda,r)}\left(\sqrt{1+\frac{32}{\sigma C_l^{\alpha}}(\beta+\theta)rF(\lambda,r)}-1\right) \tag{30}$$

The tip-loss effect on the induced inflow was considered by assuming the Prandtl's circulation loss function, $F(\lambda,r)$.

$$F(\lambda,r)=\frac{2}{\pi}\arccos\left[\exp\left(-N_b\frac{1-r}{2\lambda}\right)\right] \tag{31}$$

Finally, the inflow is computed by solving simultaneously equations (30) and (31) and used in estimation of the blade tip lift given by Eq. (29).

4.2. CENTRIFUGAL LOADING AT THE BLADE TIP

The centrifugal effects are mainly considered as being applied for the blade tip. Force acting on the mass center of the blade tip is given as

$$d\vec{F} = -dm\,\vec{\Omega} \times \left(\vec{\Omega} \times \vec{R}\right) \tag{32}$$

where the angular speed in the global reference system (inertial reference system) of the blade is

$$\vec{\Omega} = \Omega \vec{e}_Z \tag{33}$$

and the position vector in the same reference system is

$$\vec{R} = X\,\vec{e}_X + Y\,\vec{e}_Y + Z\,\vec{e}_Z \tag{34}$$

Evaluating the double cross product, the equation (32) can be rewritten as

$$d\vec{F} = dm\,\Omega^2 \left(X\,\vec{e}_X + Y\,\vec{e}_Y\right) \tag{35}$$

Corresponding moment is expressed as

$$d\vec{M} = \vec{R} \times d\vec{F} = dm\,\Omega^2 \left(-YZ\,\vec{e}_X + XZ\,\vec{e}_Y\right) \tag{36}$$

The position of the mass center for the main blade, as well as for the blade tip, was considered at 25% of chord [Ref. 3], which coincides with the aerodynamic center location. A local reference system with origin defined at the rotation center of the blade tip cross section is schematically represented in Fig. IV. 1.

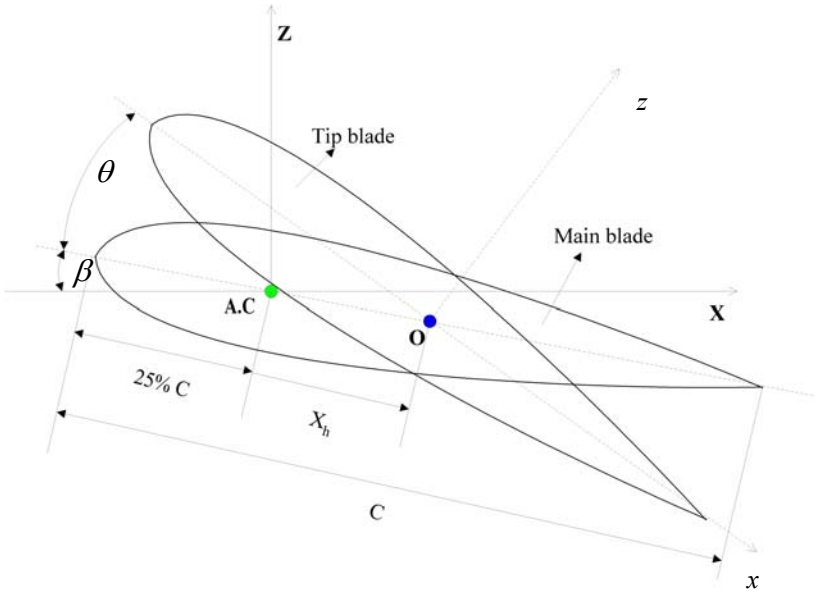

Figure IV. 1. Local reference system for blade tip cross section

The coordinate transformation between the local reference system (O*xz*) and the global reference system (OXZ) can be written as

$$\begin{cases} X = X_h \cos\beta + x\cos(\beta+\theta) + z\sin(\beta+\theta) \\ Z = -X_h \sin\beta - x\sin(\beta+\theta) + z\cos(\beta+\theta) \end{cases} \tag{37}$$

By integration of equation (35), the resulting centrifugal force acting on the blade tip mass center is

$$\vec{F}_{CF} = m\Omega^2 \left(X_c \vec{e}_X + Y_c \vec{e}_Y \right) \tag{38}$$

where $X_c = X_h\left[\cos\beta - \cos(\beta+\theta)\right]$ can be neglected for small blade tip deflection angles and Y_c represents mass center location on the blade tip span and can be approximated as *(1-0.5E)R*.

The y-direction moment about the local rotation axis is evaluated by integration of Eq. (36)

$$\vec{M}_y = J_{XZ}\, \Omega^2\, \vec{e}_Y \tag{39}$$

with the inertia moment expressed as

$$J_{XZ} = -\left(J_{XX}^C - J_{ZZ}^C\right)\frac{\sin 2(\beta+\theta)}{2} + mX_h^2(1-\cos\beta)\sin(\beta+2\theta) \tag{40}$$

where the last term can be neglected for small deflection angles. The inertia moments for NACA 0012 (which are expressed about the mass center coordinates) J_{ZZ}^{C} is much less than J_{XX}^{C}, and finally, the centrifugal moment in y-direction can be written as

$$M_y = -J_{XX}^{C}\,\Omega^2\,\frac{\sin 2(\beta+\theta)}{2} \approx -J_{XX}^{C}\,\Omega^2\,(\beta+\theta) \tag{41}$$

After a similar procedure the centrifugal moment in x-direction can be found as

$$M_x = -m\Omega^2 Y_C X_h\left[\sin(\beta+\theta)-\sin\theta\right] \approx -m\Omega^2 Y_C X_h\beta \tag{42}$$

4.3. EQUILIBRIUM EQUATION AT THE BLADE TIP

As a first step of design, the deflection angle generated through the piezoelectric actuation is evaluated when the hinge axis is considered to coincide with aerodynamic center axis. In this case the aerodynamic pitch moment is zero and the performance of the actuation is determined by the inertial effects and varies with the rotor rotational speed Ω, and with the collective pitch angle β. The constant axial load along the combined actuator is assumed since the variation of axial load along can be negligible due to the much higher centrifugal force applied on the blade tip. Because of high aspect ratio, $\frac{L_s}{2b_s}$ 10, the warping constraint effect from the fixed boundary of the combined

actuator is decayed so fast that uniform torsion is assumed. The equilibrium equation at the blade tip is shown in Eq. (43)

$$M_c(V) + M_y(\beta, \theta, \Omega) = \left[K_{coil} + K_{el} + K_F(\Omega)\right]\theta + K_{NL}\theta^3 \tag{43}$$

For the maximum applied voltage, the actuation moment generates the maximum rotation angle, which is possible when the aerodynamic pitch moment is zero.

For hinge position aft to the aerodynamic center axis, in the presence of airloads, a positive nose-up rotation of the active blade tip generates a positive aerodynamic hinge moment that tends to amplify the deflected position.

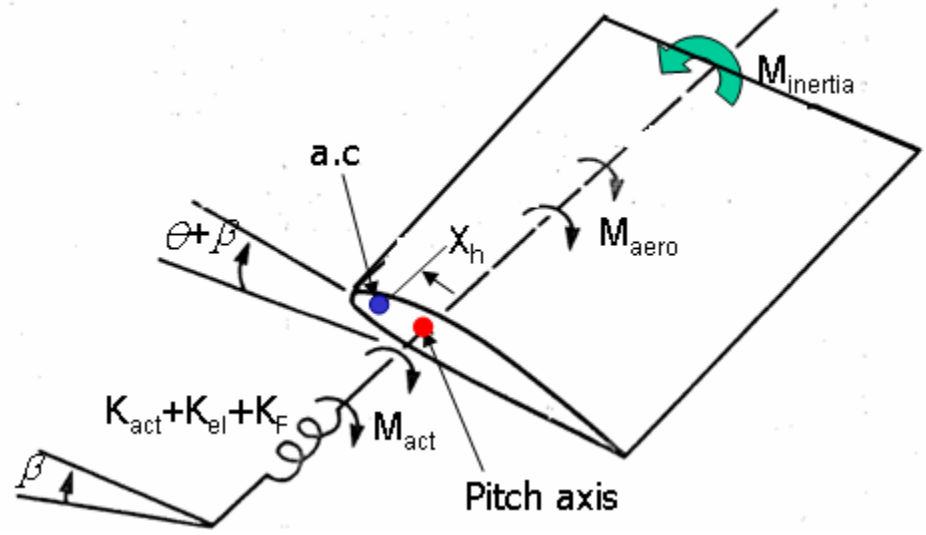

Figure IV. 2. Free body diagram of free tip

The equilibrium equation of the blade tip shown in Fig. IV. 2 becomes

$$M_c(V) + M_y(\beta,\theta,\Omega) + M_{aero}(\beta,\theta,\Omega) = \left[K_{coil} + K_{el} + K_F(\Omega)\right]\theta + K_{NL}\theta^3 \quad (44)$$

where the aerodynamic moment is given as

$$M_{aero}(\beta,\theta,\Omega) = X_h L_{aero}(\beta,\theta,\Omega) \quad (45)$$

To identify the effect of aerodynamics, the case of wing tip was analyzed, using the following simplified equilibrium equation

$$M_c(V) + M_{aero}(\beta,\theta,\Omega) = \left[K_{coil} + K_{el}\right]\theta \quad (46)$$

4.4. NUMERICAL RESULTS

4.4.1. DESIGN OF A COMBINED PIEZOELECTRIC-COMPOSITE ACTUATOR

The first design phase is to study the response of the combined actuator as a function of geometric characteristics of the helicoidal actuator. The helicoidal actuator is assumed to be made of a representative ceramic piezoelectric material, PZT-5A, with relevant characteristics given in Table IV. 1.

Table IV. 1. Piezoelectric Material Properties

E_{11}	6.1×10^{10} N/m^2
E_d	5×10^5 V/m
d_{31}	171×10^{-12} m/V

Table IV. 2. Geometric Properties of a Starbeam

No. of arms (N_s)	4
Length (L_s)	0.5 m
Width (b_s)	3.3 mm
Thickness (t_s)	6x0.156 mm

Based upon constructive considerations it is assumed that the actuator housing diameter is approximately 80% of the airfoil maximum thickness [87]. The configuration chosen for the elastic support beam is a four arms star beam made by composite material in Table III. 1 with 0 degree lay-up. The details related of material characteristics and manufacturing of composite star beams are given in Ref. [85-86]. The star beam diameter is considered approximately 90% of the housing diameter being less than the minimum diameter of the deformed actuator's coils. The geometrical characteristics of the star beam are listed in Table IV. 2. The maximal output angle is obtained when the actuator is excited with the maximum voltage admissible limited by the depoling electric field value. In Fig. IV. 3 and Fig. IV. 4, the maximal twisting angle is represented as function of

thickness and width of the actuator. The results show that for each given thickness of the actuator, the system response as function of the actuator's coil width present a local maximum response. The maximum response angle increases with the actuator thickness. Using these guiding observations, the configuration chosen for the helicoidal actuator is characterized by $t_c = 300\mu m$, $b_c = 34.6mm$ corresponding to a diameter of $7mm$ and length of $0.475mm$. The maximum applied voltage is $150V$ including a twisting angle of 4.6°.

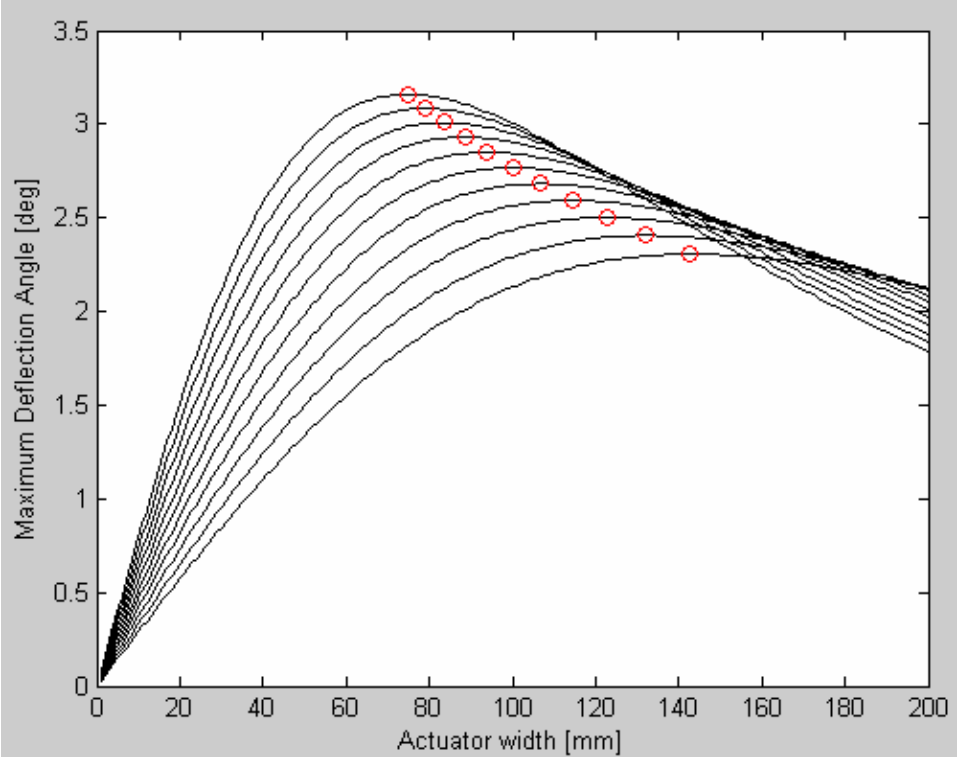

Figure IV. 3. Maximum twisting angle vs. actuator width

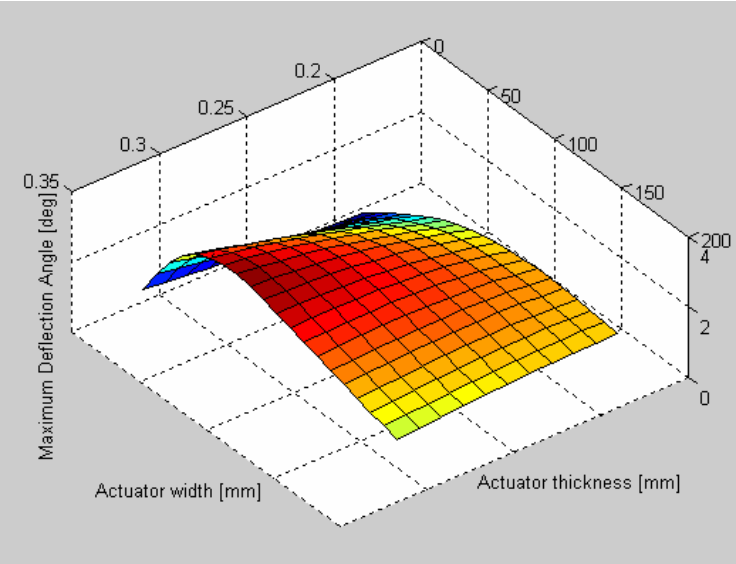

Figure IV. 4. Maximum twisting angle vs. geometric parameters of actuator

4.4.2. WING TIP DESIGN

The combined piezoelectric-composite actuator is considered rigidly attached to the blade tip. To analyze the aerodynamic effect over the coupled actuator and tip blade, the wing case was considered. Same type of airfoil section is used at both case and the geometric properties of wing/blade main model and tip model are listed in Table IV. 3 and Table IV. 4. Depending on the hinge position, the tip wing deflection can be amplified or reduced. When the hinge axis is situated at 25% chord, the hinge point for the wing section coincides with the aerodynamic center for the incompressible flow regime and the aerodynamic pitch moment is zero. Moving the hinge position aft to aerodynamic center, the wing tip response is amplified by aerodynamic moment and in the limit the divergence phenomenon can occur. In Fig. IV. 5 and Fig. IV. 6, the tip deflection responses at applied voltage corresponding to 0 and 4 degree of pitch angle are

represented for a wing configuration characterized by a hinge position 0.5% chord aft aerodynamic center. They show the effects of Mach number and applied voltage on the maximum wing tip deflection angle in case of pitch angles of 0 and 4. DYMORE result is reasonably following the trend of the analytical results. Figure IV. 7 shows the DYMORE model of a half wing span.

Table IV. 3. Main Wing/Blade Model's Properties

Parameters	Value
Airfoil shape	NACA 0012
Aspect ratio (AR)	12
Chord length (c)	0.0762 m
Lift curve slope (C_l^{α})	0.1075
Housing radius (r_{hole})	0.0037 m

Table IV. 4. 10% Span Wing/Blade Tip Model's Properties

Parameters	Value
Airfoil Shape	NACA 0012
Lift curve slope (C_l^{α})	0.1075
Mass (m)	0.0425 kg
Pitch inertia (J_{xx})	8.34×10^{-6} kgm^2
Mass center (Y_c)	25% chord length

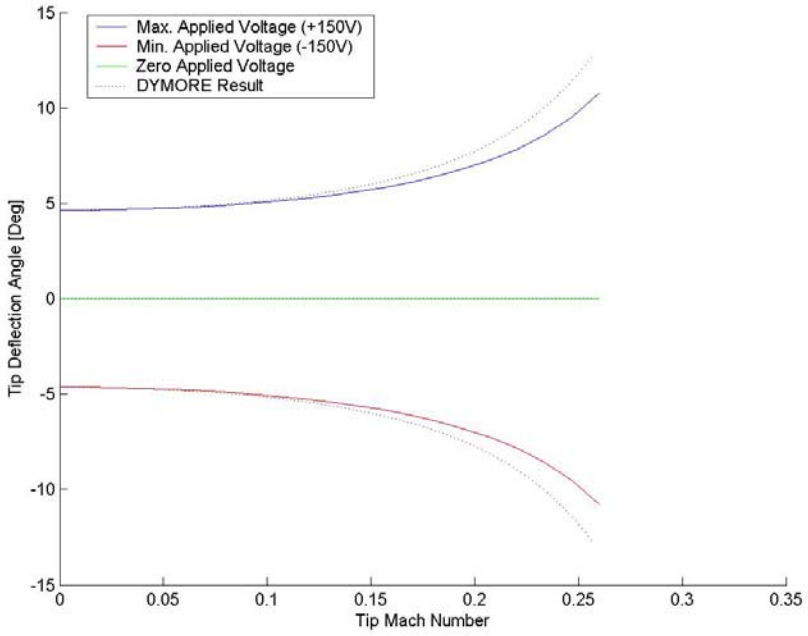

Figure IV. 5. Wing tip deflection angle with the pitch angle of 0 degree with respect to tip Mach number (starbeam)

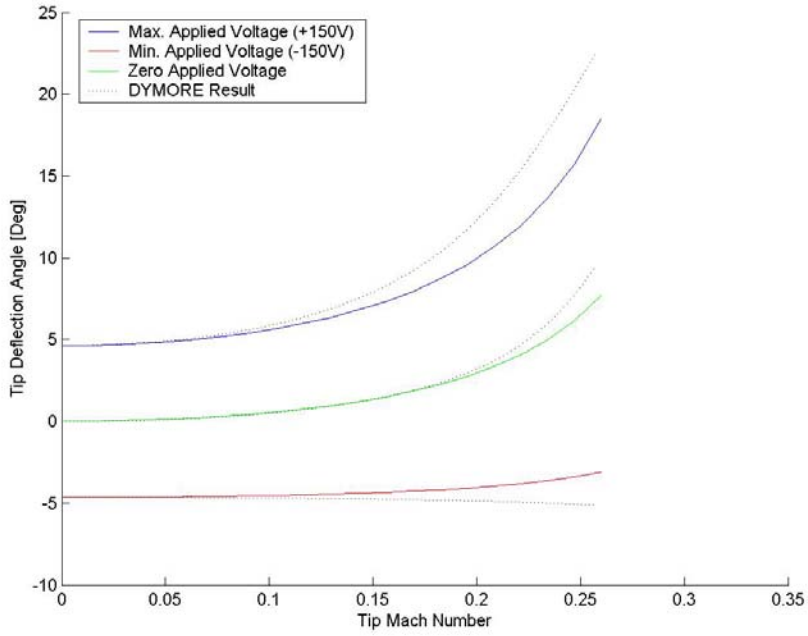

Figure IV. 6. Wing tip deflection angle with the pitch angle of 4 degree with respect to tip Mach number (starbeam)

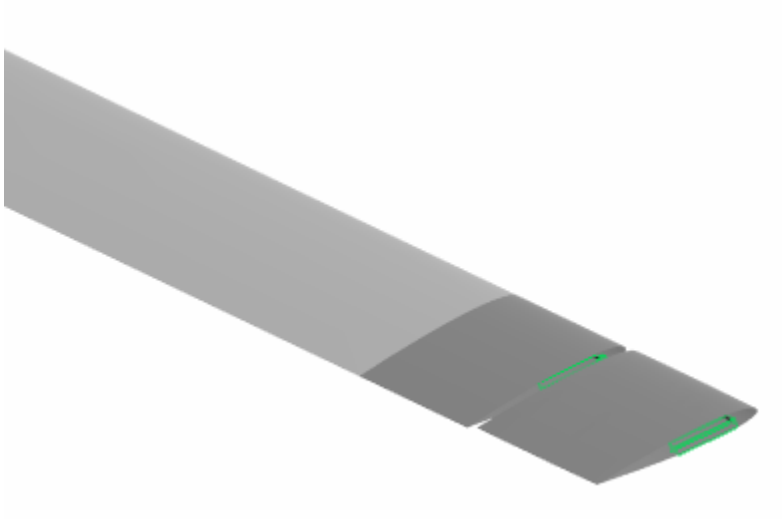

Figure IV. 7. DYMORE model of half span wing

The range of output response is positively shifted with the angle of attack, as $a.o.a = 0^\circ$, $\theta \in [-11.3, +11.3]$, $a.o.a = 4^\circ$, $\theta \in [-2.8, +19.8]$, and $a.o.a = 8^\circ$, $\theta \in [+5.7, +28.3]$ corresponding to a free stream Mach of 0.26. For the configuration chosen the aerodynamic effect is benefic for small angles of attack, enlarging the range of wing tip response, However, for higher angle of attack the shifted response is too high and does not include any more the required design range $\theta \in [-2, +2]$.

Fig. IV. 8 and Fig. IV. 9 explain more details about effect of Mach number and applied voltage to wing tip angle corresponding to 0 and 4 degree of pitch angle. It shows that as applied voltage increases maximum deflection angle increases while maximum deflection angle is depending on the pitch angle because of angle of attack effect on direction of lift force.

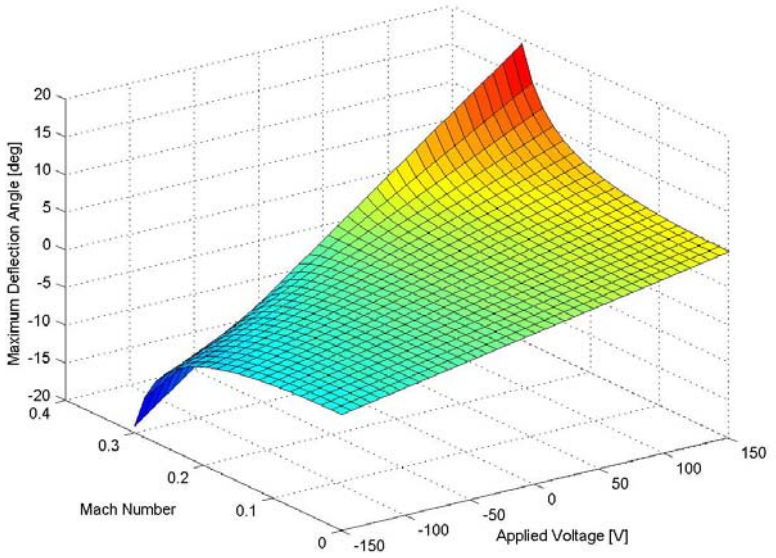

Figure IV. 8. Maximum deflection angle of a wing tip with the pitch angle of 0 degree with respect to applied voltage and tip Mach number

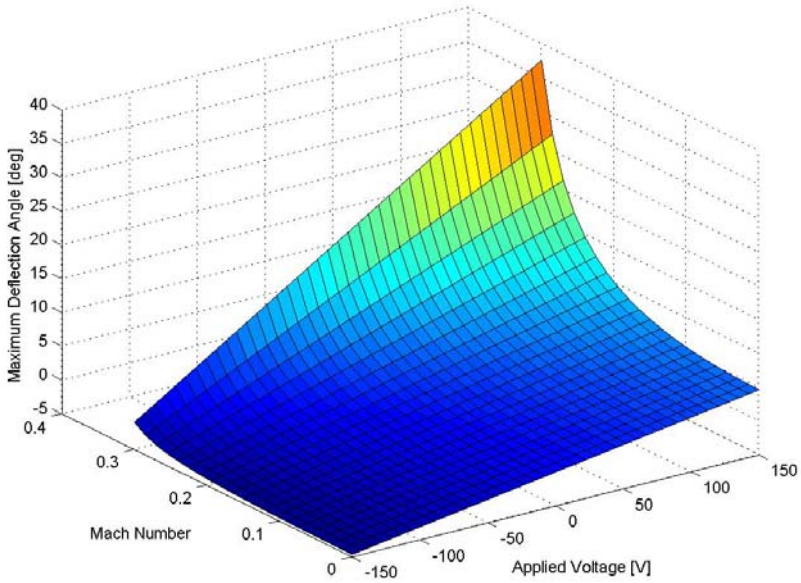

Figure IV. 9. Maximum deflection angle of a wing tip with the pitch angle of 4 degree with respect to applied voltage and tip Mach number

4.4.3. BLADE TIP DESIGN

In the case of rotor blade, the centrifugal effects cause torsional stiffening of the elastic structure and occurrence of a restoring pitch moment due to blade tip inertia. As in previous analysis for the wing tip, the aerodynamic effects are related to the hinge axis position. When the hinge position is at 25% chord (X_h =0.0), the aerodynamic pitch moment is zero and only the inertial effects perturb the blade tip response. In this chapter, the response of blade tip using starbeam as an hinge bar is considered first, then the response of blade tip using modified starbeam considered, and then parametric analysis will be discussed later. A snapshot of rotorcraft blade simulation from DYMORE and the detailed schematic design of rotorcraft blade including moving tip in DYMORE are shown in Fig. IV. 10 and Fig. IV. 11, respectively.

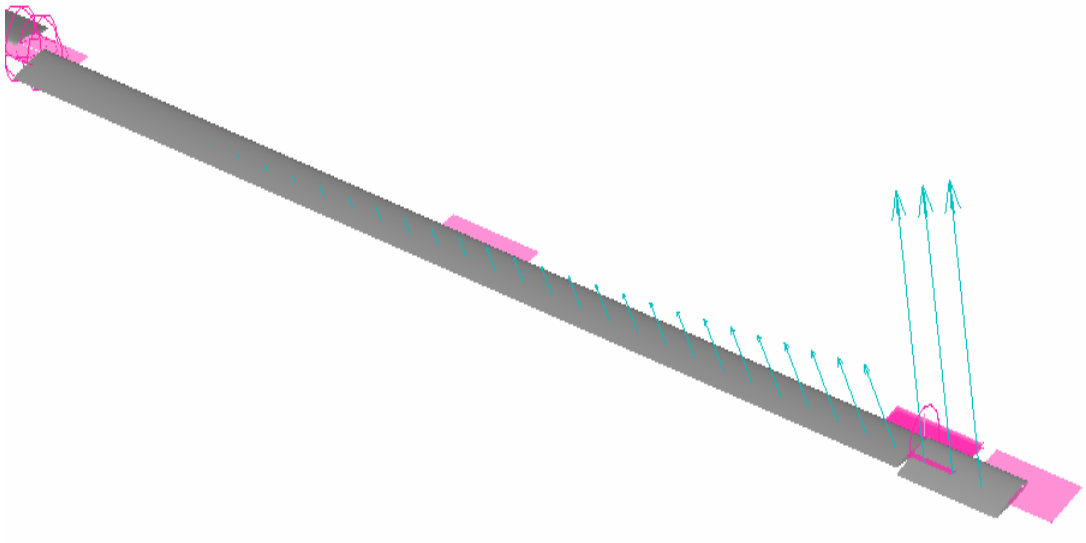

Figure IV. 10. DYMORE model of rotorcraft blade with moving tip

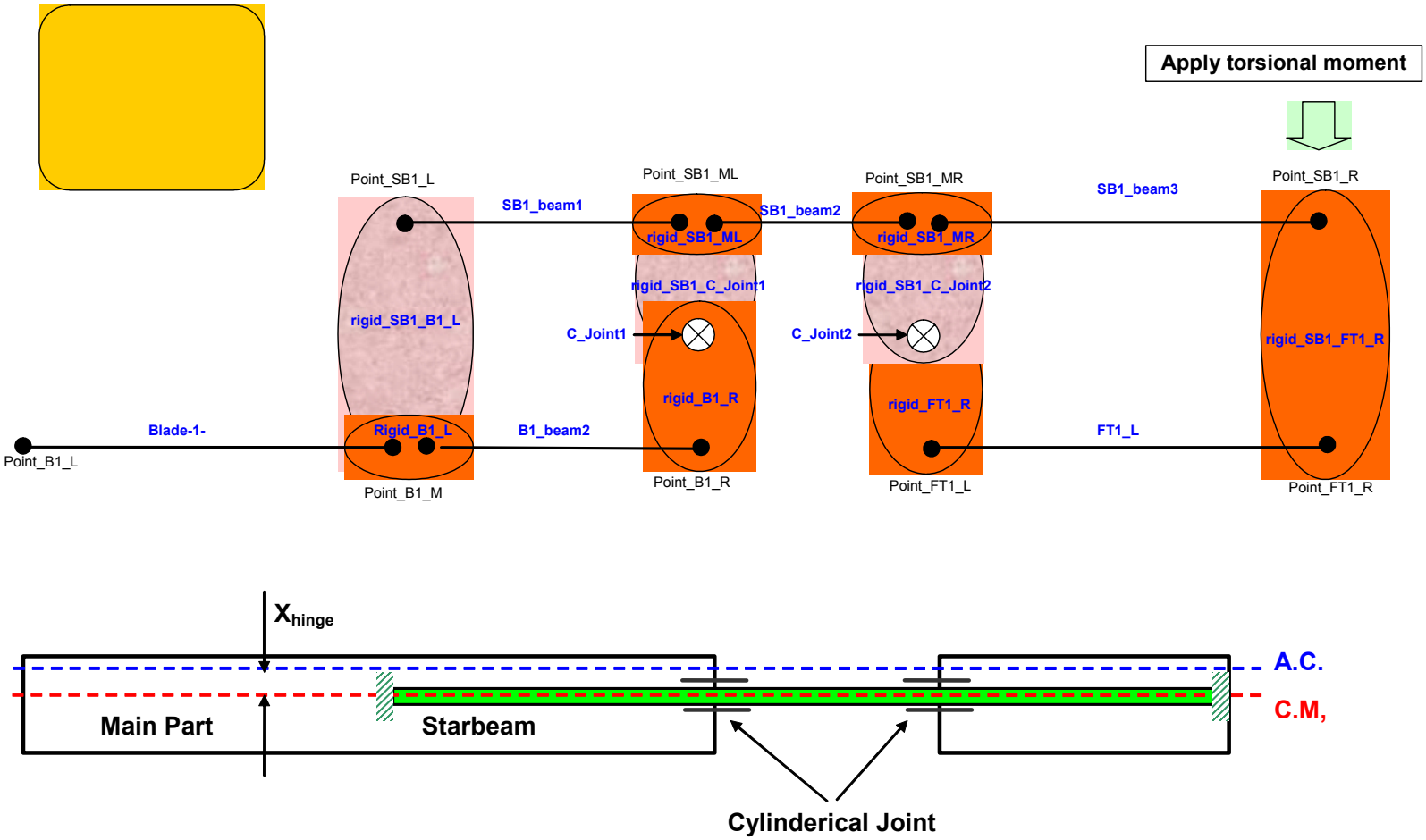

Figure IV. 11. Schematic design of blade tip model in DYMORE

4.4.3.1. BLADE TIP DESIGN USING STARBEAM AS AN HINGE BAR

The geometrical characteristics of a starbeam are listed in Table IV. 2. In Fig. IV. 12 and Fig. IV. 13, the curve responses for blade tip deflection angle are represented for pitch angles of 0 and 4 degrees. The curve response for zero applied voltage represents the case of free tip. Results from DYMORE are also shown in Fig. IV. 12 and Fig. IV. 13, which show good correlation with analytical results. In DYMORE, static analysis was used to find tip angle of helicopter with 2 blades.

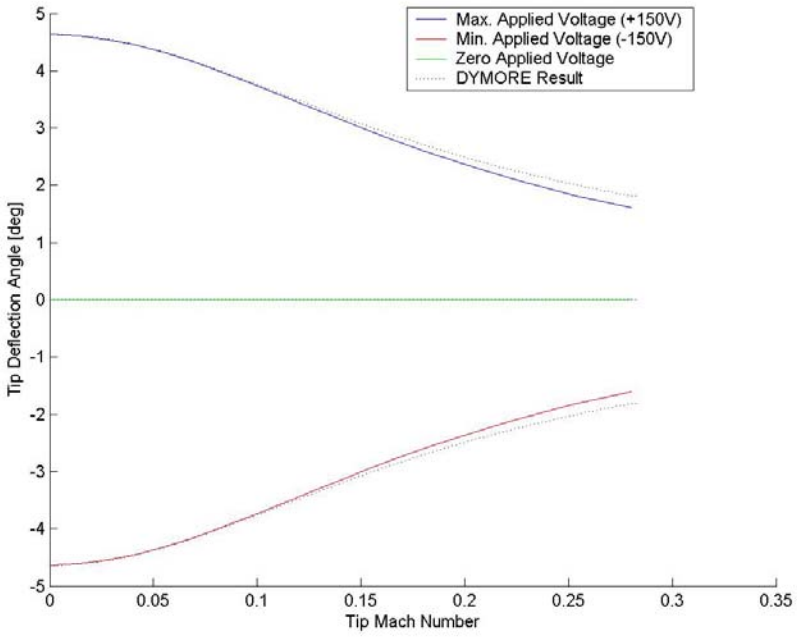

Figure IV. 12. Blade tip deflection angle with hinge location of 0.0% chord length and pitch angle of 0 degree with respect to tip Mach number (starbeam)

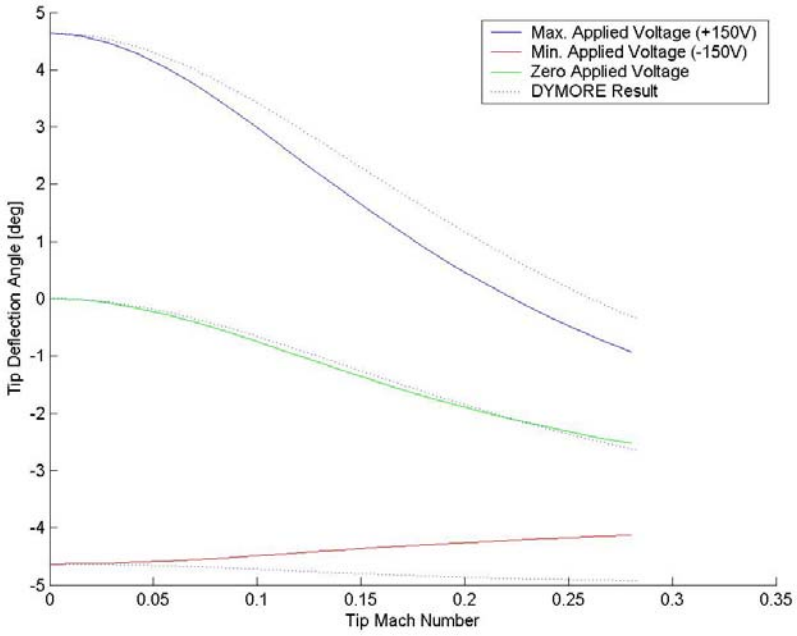

Figure IV. 13. Blade tip deflection angle with hinge location of 0.0% chord length and pitch angle of 4 degree with respect to tip Mach number (starbeam)

Table IV. 5. Blade Tip Deflection Range for X_h=0.0% chord length

Collective pitch angle (C.P.A.)		Moving tip angle w.r.t. C.P.A. (V=-150Volt)	Moving tip angle w.r.t. C.P.A. (V=+150Volt)	Moving tip angle w.r.t. C.P.A. (V=0Volt)
0º	Analytical Result	-1.8º	+1.8º	0º
	Dymore Result	-1.81º	+1.81º	0º
	Absolute Error	0.01º	0.01º	0º
4º	Analytical Result	-4.2º	-0.6º	-2.4º
	Dymore Result	-4.9º	-0.2º	-2.62º
	Absolute Error	0.7º	0.4º	0.22º

The blade tip deflection ranges corresponding to Mach tip of 0.26 are listed in Table IV. 5 for different pitch angles and hinge location of 25% chord (X_h =0.0). In Fig. IV. 14 – Fig. IV. 17, the curve responses for blade tip deflection angle are represented when hinge position is aft aerodynamic center with 1% chord and 1.5% chord, respectively. DYMORE result also was compared with analytical results in the same figures. The corresponding blade tip deflection ranges for Mach tip of 0.26 are listed in Table IV. 6 and Table IV. 7 for different pitch angles of 0 and 4 degree. The results listed in Table IV. 6 and Table IV. 7, show the benefit of hinge position aft aerodynamic center, such that the blade tip response is positive by airloads. Opposite, the centrifugal effects cause a negative shifting of the response domain of β. Adding these effects determines a beneficial enlarging of blade tip response domain. The results for X_h=1.5% chord, configuration proves that the designed range $\beta \in [-2,+2]$ can be achieved for all pitch angle configurations chosen.

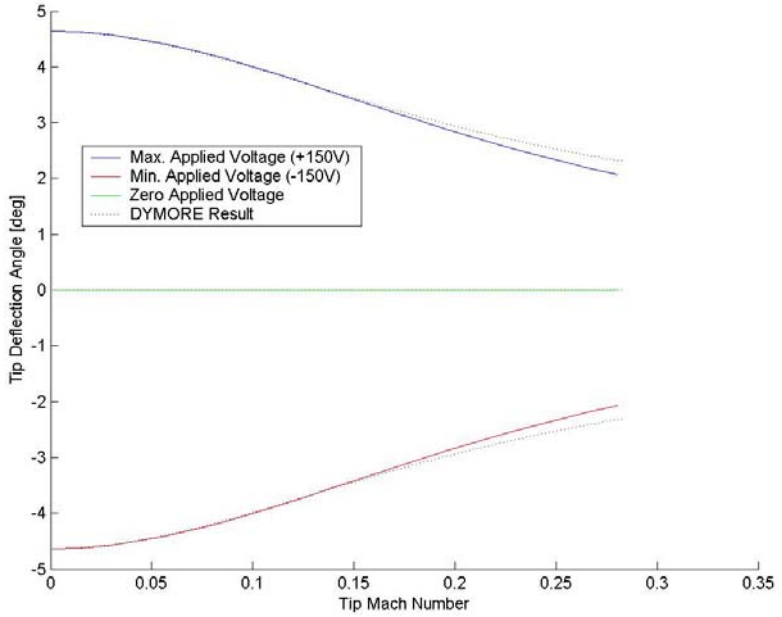

Figure IV. 14. Blade tip deflection angle with hinge location of 1.0% chord length and pitch angle of 0 degree with respect to tip Mach number (starbeam)

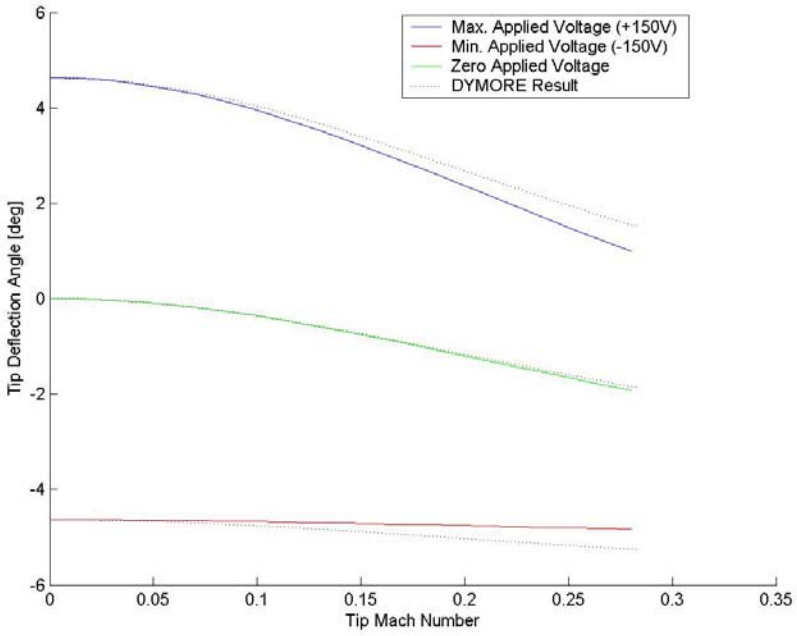

Figure IV. 15. Blade tip deflection angle with hinge location of 1.0% chord length and pitch angle of 4 degree with respect to tip Mach number (starbeam)

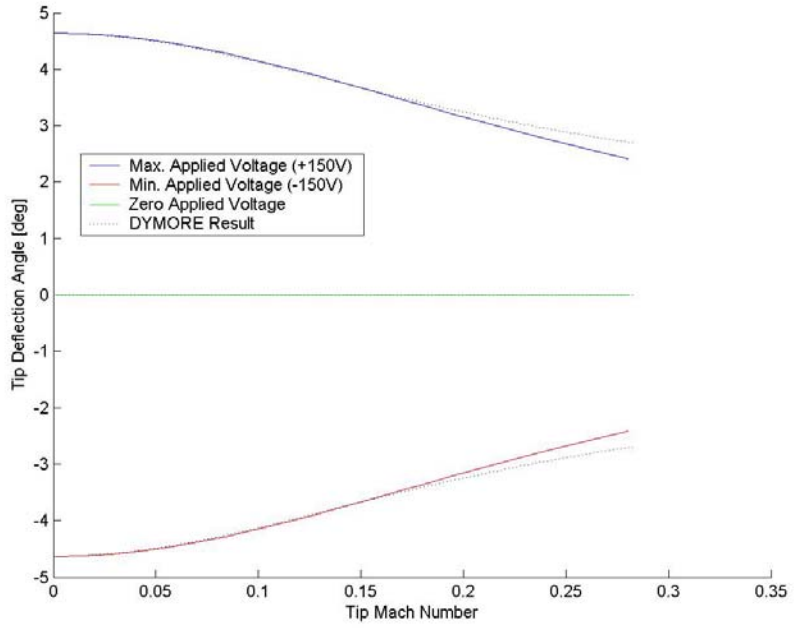

Figure IV. 16. Blade tip deflection angle with hinge location of 1.5% chord length and pitch angle of 0 degree with respect to tip Mach number (starbeam)

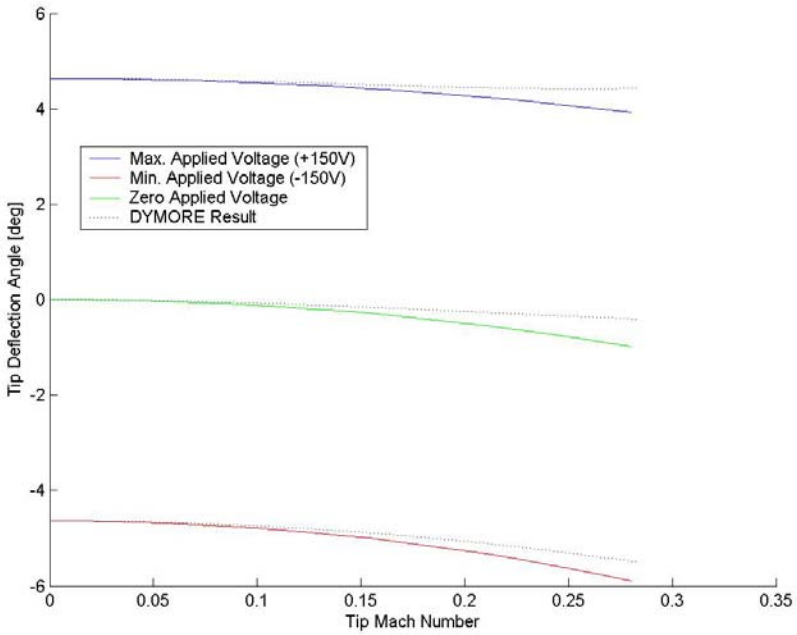

Figure IV. 17. Blade tip deflection angle with hinge location of 1.5% chord length and pitch angle of 4 degree with respect to tip Mach number (starbeam)

Table IV. 6. Blade Tip Deflection Range for X_h=1% chord length

Collective pitch angle (C.P.A.)		Moving tip angle w.r.t. C.P.A. (V=-150Volt)	Moving tip angle w.r.t. C.P.A. (V=+150Volt)	Moving tip angle w.r.t. C.P.A. (V=0Volt)
0º	Analytical Result	-2.2º	+2.2º	0º
	Dymore Result	-2.32º	+2.32º	0º
	Absolute Error	0.12º	0.12º	0º
4º	Analytical Result	-4.8º	+1.3º	-1.7º
	Dymore Result	-5.25º	-1.67º	-1.8º
	Absolute Error	0.45º	0.37º	0.1º

Table IV. 7. Blade Tip Deflection Range for X_h=1.5% chord length

Collective pitch angle (C.P.A.)		Moving tip angle w.r.t. C.P.A. (V=-150Volt)	Moving tip angle w.r.t. C.P.A. (V=+150Volt)	Moving tip angle w.r.t. C.P.A. (V=0Volt)
0º	Analytical Result	-2.6º	+2.6º	0º
	Dymore Result	-2.7º	+2.7º	0º
	Error (%)	0.1º	0.1º	0º
4º	Analytical Result	-5.7º	+4.0º	-0.8º
	Dymore Result	-5.5º	+4.43º	-0.41º
	Error (%)	0.2º	0.43º	0.39º

4.4.3.2. BLADE TIP DESIGN USING MODIFIED STARBEAM AS AN HINGE BAR

An alternative modified starbeam configuration with same area with as original starbeam was analyzed considering the same characteristics of the actuator. The geometrical characteristics of this modified starbeam are listed in Table IV. 8.

This configuration is characterized by a higher torsional flexibility, the maximum twisting angle obtained for a combined piezoelectric composite actuator system being of 6.7 with 2 degrees higher the similar value obtained for the simple starbeam.

Table IV. 8. Geometric Properties of a Modified Starbeam

No. of arms (N_s)	4
Length (L_s)	0.5 m
Arc Angle (α)	0.16 rad
Width (b_s)	3.3 mm
Thickness (t_s)	4x0.156 mm

In Fig. IV. 18 – Fig. IV. 21, the curve responses for blade tip deflection angles are represented when hinge position coincides with aerodynamic center and when hinge position is aft aerodynamic center with 0% and 1.5% chord. In the same way, DYMORE results are also compared with analytical results in the same figures. The corresponding blade tip deflection ranges for Mach tip of 0.26 are listed in Table IV. 9 and Table IV. 10

for different pitch angles, 0 and 4 degree. The comparison of these results with the similar results listed in Table IV. 5 – Table IV. 7, reveals the benefit of using the modified star shape cross sectional beam configurations as more flexible supports for the blade tips.

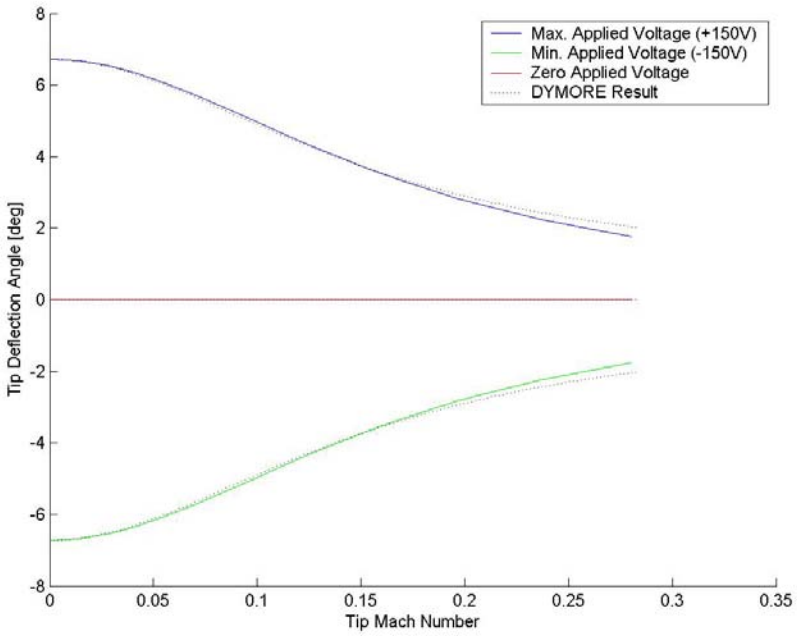

Figure IV. 18. Blade tip deflection angle with hinge location of 0.0% chord length and pitch angle of 0 degree with respect to tip Mach number (modified starbeam)

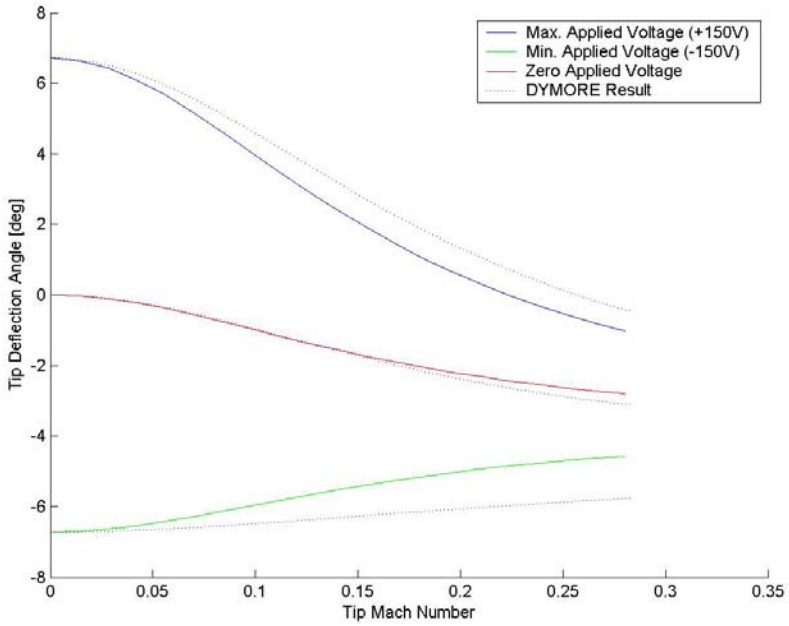

Figure IV. 19. Blade tip deflection angle with hinge location of 0.0% chord length and pitch angle of 4 degree with respect to tip Mach number (modified starbeam)

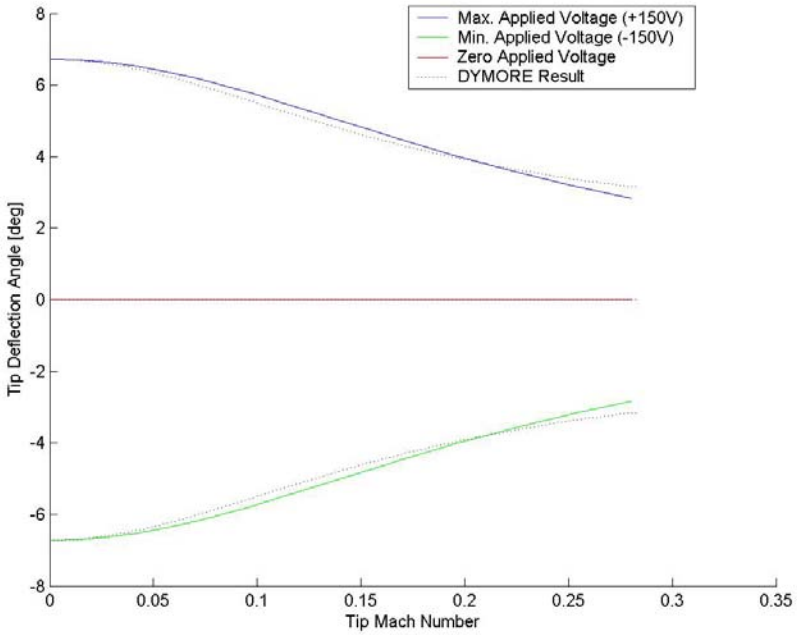

Figure IV. 20. Blade tip deflection angle with hinge location of 1.5% chord length and pitch angle of 0 degree with respect to tip Mach number (modified starbeam)

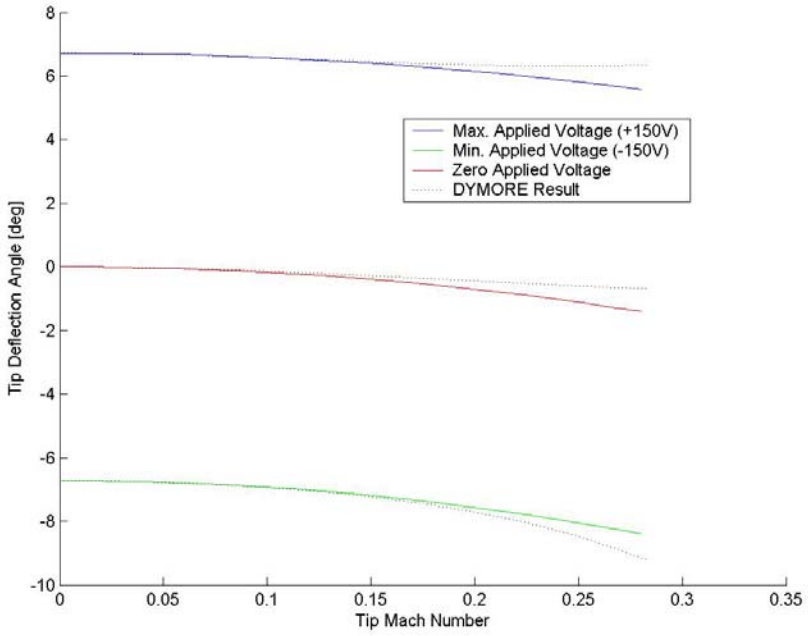

Figure IV. 21. Blade tip deflection angle with hinge location of 1.5% chord length and pitch angle of 4 degree with respect to tip Mach number (modified starbeam)

Table IV. 9.Blade Tip Deflection Range for X_h=0.0% chord length

Collective pitch angle (C.P.A.)		Moving tip angle w.r.t. C.P.A. (V=-150Volt)	Moving tip angle w.r.t. C.P.A. (V=+150Volt)	Moving tip angle w.r.t. C.P.A. (V=0Volt)
0º	Analytical Result	-2.0º	+2.0º	0º
	Dymore Result	-2.05º	+2.05º	0º
	Absolute Error	0.05º	0.05º	0º
4º	Analytical Result	-4.7º	-0.7º	-2.7º
	Dymore Result	-5.7º	-0.3º	-3.0º
	Absolute Error	1.0º	0.4º	0.3º

Table IV. 10. Blade Tip Deflection Range for X_h=1.5% chord length

Collective pitch angle (C.P.A.)		Moving tip angle w.r.t. C.P.A. (V=-150Volt)	Moving tip angle w.r.t. C.P.A. (V=+150Volt)	Moving tip angle w.r.t. C.P.A. (V=0Volt)
0º	Analytical Result	-3.08º	+3.08º	0º
	Dymore Result	-3.15º	+3.15º	0º
	Absolute Error	0.07º	0.07º	0º
4º	Analytical Result	-8.2º	+5.74º	-1.2º
	Dymore Result	-8.1º	+6.14º	-0.7º
	Absolute Error	0.1º	0.4º	0.5º

5.4.3.1. PARAMETRIC ANALYSIS

A. Length of modified starbeam

As the ratio of the length of modified starbeam to blade length increase, the torsional stiffness of the modified starbeam at the blade tip is decreased and tip deflection angle increased shown in Fig. IV. 22 and Fig. IV. 23. Both figures also show that the increasing rate of tip deflection angle depends on the pitch angle of the rotorcraft blade. It can be addressed that the length of modified starbeam having a half length of blade is good for improving lift performance as well as avoiding stall of NACA 0012 airfoil.

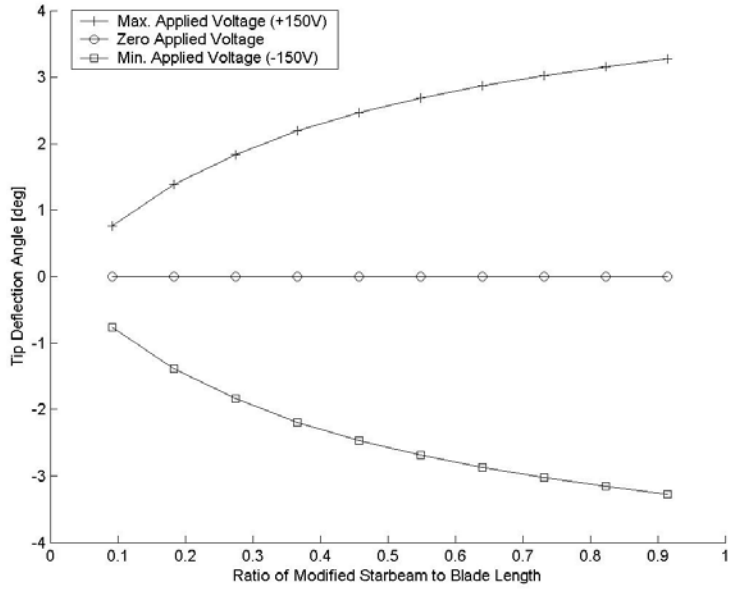

Figure IV. 22. Blade tip deflection angle with hinge location of 1.5% chord length and pitch angle of 0 degree with respect to ratio of modified starbeam to blade length

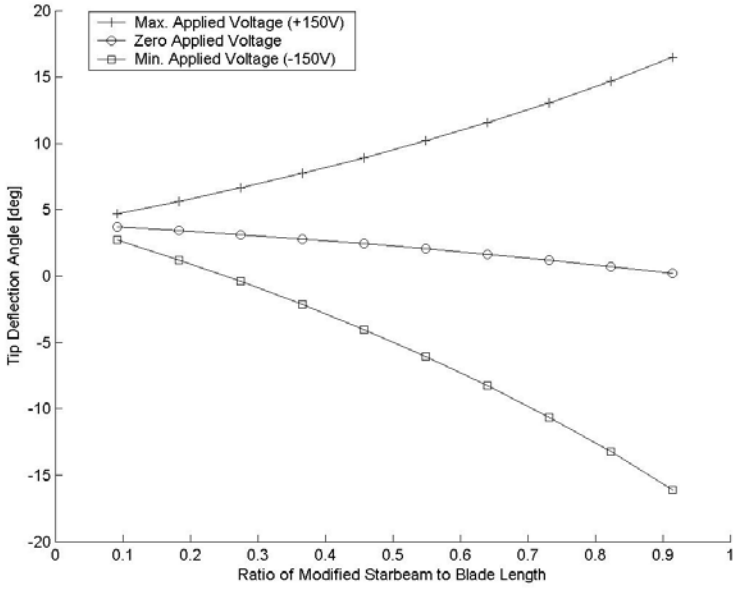

Figure IV. 23. Blade tip deflection angle with hinge location of 1.5% chord length and pitch angle of 4 degree with respect to ratio of modified starbeam to blade length

B. Hinge location of modified starbeam

Hinge location of the modified starbeam along the chord length at the blade tip is very important factor because it can cause the failure of modified starbeam strength and performance improvement resulting from undesirable high tip deflection angle shown in Fig. IV. 24 and Fig. IV. 25, especially for high pitch angle of blade. From both figures 1.5% value of hinge location is proper for both pitch angles of 0 and 4 degree.

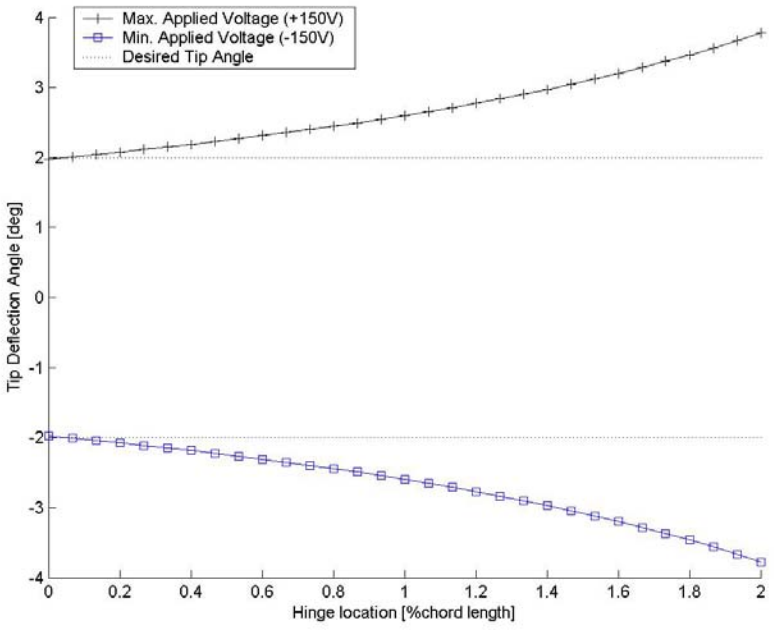

Figure IV. 24. Blade tip deflection angle with 0.26 valued Mach number and pitch angle of 0 degree with respect to hinge location of modified starbeam

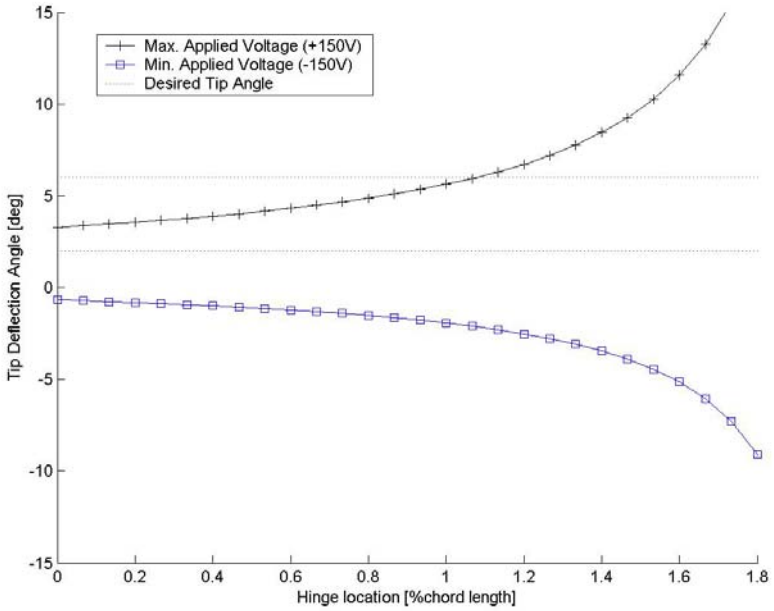

Figure IV. 25. Blade tip deflection angle with 0.26 valued Mach number and pitch angle of 4 degree with respect to hinge location of modified starbeam

C. Inertial effects on blade tip deflection angle

Inertial effects on blade tip deflection angle with different pitch angles of 0 and 4 degree are shown in Fig. IV. 26 and Fig. IV. 27. Torsional stiffening effect and tennis-racquet effect due to centrifugal force are represented in the dotted line without aerodynamic effect in both figures. As pitch angle attack of the blade becomes increased, aerodynamic load gives more influence on the tip deflection angle than inertial effect does.

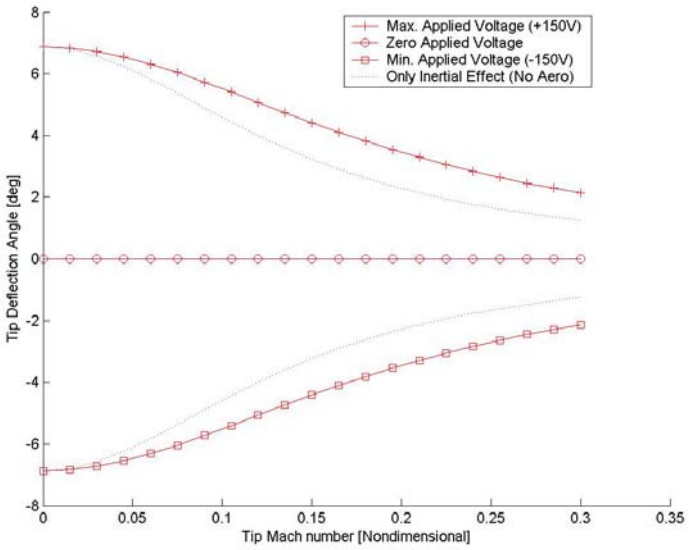

Figure IV. 26. Inertia effect to tip deflection angle with hinge location of 1.5% chord length and pitch angle of 0 degree with respect to tip Mach number (modified starbeam)

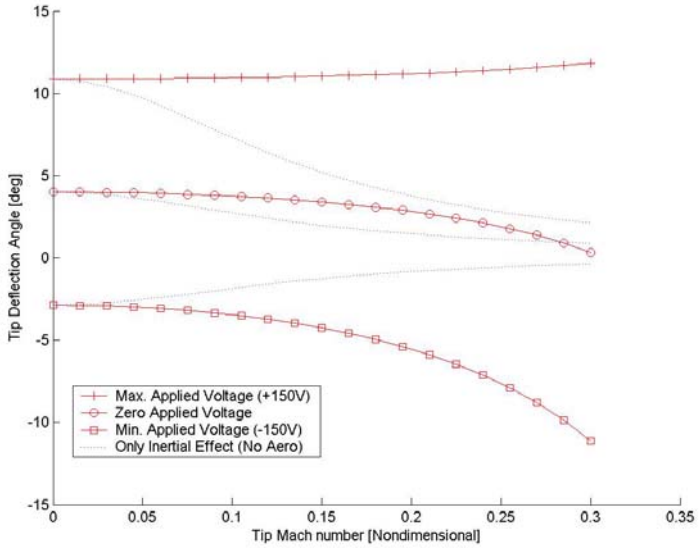

Figure IV. 27. Inertia effect to tip deflection angle with hinge location of 1.5% chord length and pitch angle of 0 degree with respect to tip Mach number (modified starbeam)

D. Pitch Angle of the Blade

Fig. IV. 28 shows that increasing pitch angle of blade increases blade tip deflection angle. It also state that higher pitch angle can cause blade tip stall and other non beneficial effect on the performance.

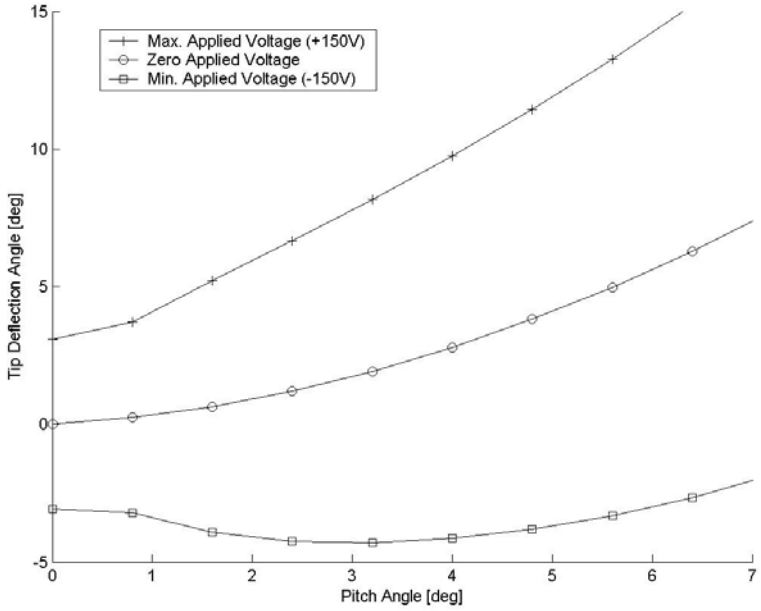

Figure IV. 28. Blade tip deflection angle with hinge location of 1.5% chord length and 0.26 valued Mach number with respect to pitch angle of the blade

E. Comparison of stiffness ratio of torsional stiffness due to centrifugal force to elastic stiffness of starbeam with that of a modified starbeam

Fig. IV. 29 shows the inertia effects on the torsional stiffness of starbeam and modified starbeam. It was found that the ratio between torsional stiffness due to centrifugal effects and elastic stiffness is about 10% in case of starbeam while 31.9% in case of modified starbeam with Mach tip of 0.26, which means that the inertial effects become more predominant for modified starbeam configuration.

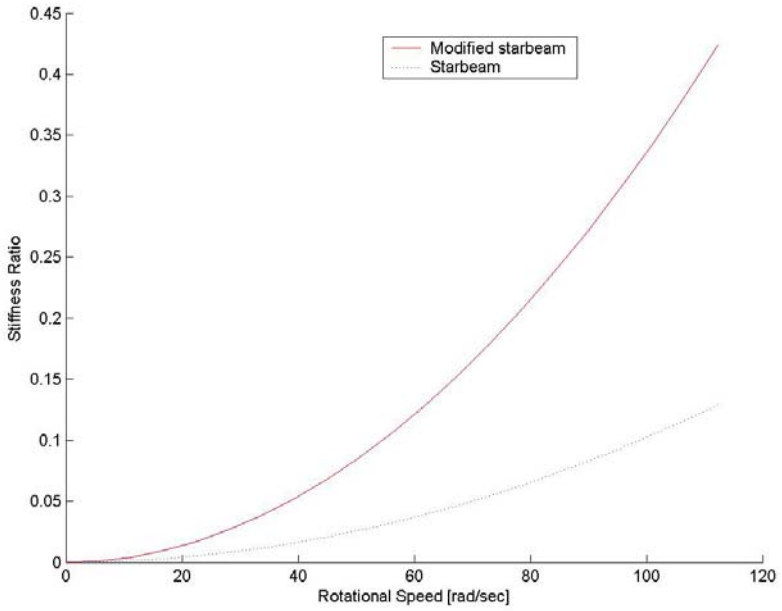

Figure IV. 29. Comparison of stiffness ratio of torsional stiffness due to centrifugal force to elastic stiffness of starbeam with that of a modified starbeam with hinge location of 1.5% chord length and pitch angle of 4 degree

CHAPTER V

CONCLUSIONS AND RECOMMENDATIONS FOR FUTURE WORK

A novel combined piezoelectric-composite actuator configuration was proposed and modeled analytically and numerically in this work. The actuator is a low complexity, active compliant mechanism obtained by coupling a modified star cross sectional configuration composite beam with a helicoidal bimorph piezoelectric actuator coiled around it. The modified star beam is tailored and optimized to achieve increased torsional compliance and bending stiffness at given constant axial stiffness. The coiled piezoelectric actuator is designed to directly generate finite rotation output without the need for mechanisms to amplify the piezoelectric displacement output and/or convert linear output to rotational output. The proposed cylindrical actuator configuration is compact and is a good candidate for use as a hinge tension-torsion bar actuator for a helicopter rotor blade flap or blade tip. For such cases the modified star composite beam also carries the centrifugal loads of the flap or blade tip, and those of the coiled actuator, thereby eliminating the need for a thrust bearing. Consequently, friction/sticktion and backlash effects that represent difficulties commonly encountered by other induced strain blade actuation configurations are eliminated.

In this work, the analytical model of a modified star beam was developed and its axial, bending and torsional stiffness were compared with those of ABAQUS and SVBT.

It showed that the analytical model based on thin walled beam theory had good agreement with numerical results from ABAQUS and SVBT, so is simple yet good enough to be used further.

Compared to a small radius cylindrical steel rod geometrically, star beam configurations with same cross sectional area have high axial and bending stiffness but low torsional stiffness. Use of composite material gives additional benefits of flexibility and low density in a material aspect. In addition to geometric and material changes, the tailoring of elastic properties by using 0 degree fiber orientation degree gives also higher axial and bending stiffness while keeping lower torsional stiffness than those of star shaped steel beam.

As shown in comparison of stiffness values between a star configuration beam and a modified star configuration beam, an optimized modified star composite beam is more suitable to tension torsion bar than a star composite beam because of additional higher bending stiffness and lower torsional stiffness.

A combined piezoelectric-composite actuator can be obtained by loosely coiling a helicoidal bender around a modified star beam and connecting two component through a set of pinned points, such that subject to axial loads the piezoelectric actuator is transferred to the modified star beam.

The analytical model of the combined piezoelectric composite actuator was developed under combined loading and applied voltage. The tip twist of the actuator under combined loading is smaller not only than the value for the helicoidal coil alone but also than that of the combined actuator subjected to no axial loading because of torsional stiffness of starbeam itself and apparent torsional stiffness due to axial loading.

The combined piezoelectric composite actuator was applied to a helicopter blade tip and a wing tip in order to investigate the response. In the wing tip case, the tip deflection angle is different only according to aerodynamic moment depending on hinge position of the actuator along the chord and applied voltage because there is no centrifugal force.

For an active blade tip under the condition of incompressible flow and 2D quasi steady airloads, its twist angle is related to not only aerodynamic moment and applied voltage but also coupling terms, trapeze effect and tennis racquet effect. Results showed the benefit of hinge position aft of the aerodynamic center, such that the blade tip response is amplified by airloads. Opposite, the centrifugal effects and inertial effect cause a negative shifting of the response domain. Adding these effects determines a beneficial enlarging of blade tip response domain. The results for a certain hinge position X_h=1.5% chord configuration proves that the design range $\beta \in [-2,+2]$ can be achieved for all pitch angle configurations chosen.

In conclusion, a novel combined piezoelectric-composite actuator configuration comprising a coiled bender actuator and a modified star shaped composite beam has been analyzed and considered under a combined loading. The potential of this new actuator to wing/blade tips in order to improve performance has been shown.

The research presented in this thesis points to new areas of inquiry. The recommended research areas for future work are

1. Dynamic response of a combined piezoelectric composite actuator with proposed configuration in a rotating frame loading to isolate aeroelastic effects.

2. Fatigue behavior of a wing/blade tips which are pertinent to rotorcraft and aircraft applications.

3. Investigation of stability from high pitch angle of wing/blade tips which might happen due to the low torsional stiffness of a combined piezoelectric composite actuator.

4. Mach scale design of a rotor with active blade tips using a combined piezoelectric composite actuator proposed and experimental verification with analytical and numerical results.

5. Wind tunnel test to investigate noise reduction due to smooth or rapid change in airflow near blade tip resulting from static or dynamic moving of blade tip.

APPENDIX A

ANALYSIS OF A THIN WALLED BEAM WITH CONSTANT AXIAL LOAD AND TIP TORQUE

Under the constant axial load and tip torque, the beam is subjected to an extension-twist coupled stresses, the shear effect being neglected in this preliminary work. The analytical expression for the thin walled laminated composites exhibiting extension-twist coupling was developed by Armanios, Makeev and Hooke in Ref. 81. Instead of the full analytical solution obtained in Ref. 81, the simplified expression of the beam response is considered. The obtained form consists of elastic torsional stiffness, the apparent torsional stiffness due to axial load and the nonlinear term identified as due to trapeze effect [82].

The undeformed and deformed configurations of the general thin walled cross sectional beam are shown in Fig. A. 1 and the deformed length of element length A_0B_0 is given by

$$\left|A_0B_1\right| = \sqrt{\left(\Delta y + \varepsilon_0 \Delta y\right)^2 + \left(r\Delta\theta\right)^2} = \Delta y\sqrt{\left(1+\varepsilon_0\right)^2 + r^2\phi^2} \qquad \text{(A-1)}$$

where, Δy is the differential length of the element, ε_0 is axial strain expressed in the undeformed axis. r is the distance of the particle from the centroid, and ϕ is twist rate ($=\frac{\Delta\theta}{\Delta y}$).

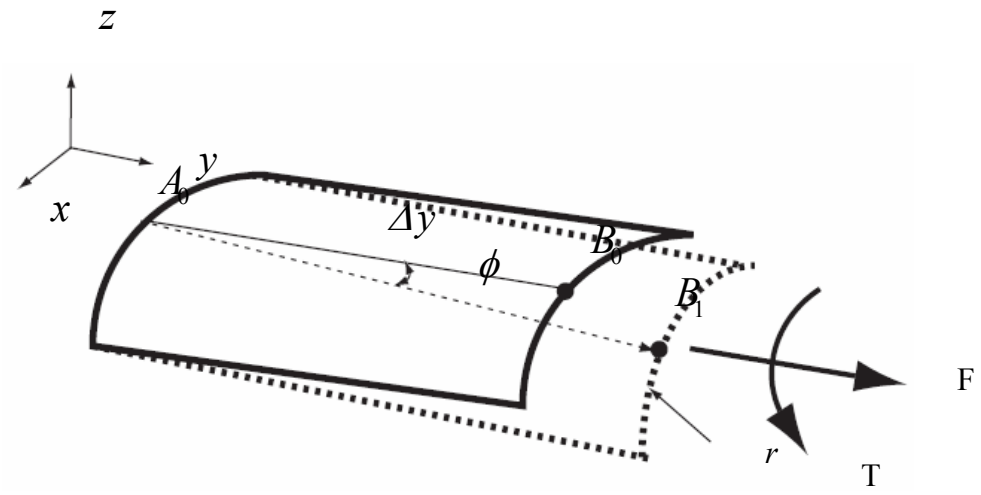

Figure A. 1. Undeformed (solid line) and deformed (dot line) configurations of the thin walled beam

From the definition, strain in the deformed axis is given by

$$\varepsilon = \frac{|A_0B_1| - \Delta y}{\Delta y} = \sqrt{(1+\varepsilon_0)^2 + r^2\phi^2} - 1 \approx \varepsilon_0 + \frac{r^2\phi^2}{2} \qquad \text{(A-2)}$$

The sectional resultant force is then obtained by

$$F = \int_{Area} \sigma_{11} dA = \int_{Area} E_{11}\left(\varepsilon_0 + \frac{r^2\phi^2}{2}\right)dA = E_{11}\varepsilon_0 A + E_{11} I_2 \frac{\phi^2}{2} \tag{A-3}$$

where A is the sectional area of the thin-walled beam and I_2 is the second moment of area of the beam section.

Also, resultant twisting moment is sought by

$$\begin{aligned} T &= \int_{Area} \tau\, r\, dA = \int_{Area} (\tau_0 + \sigma\, r\phi) r dA = \int_{Area} \tau_0\, r\, dA + \int_{Area} E_{11}\left(\varepsilon_0 + \frac{r^2\phi^2}{2}\right)\phi r^2 dA \\ &= (GJ)_{star}\phi + E_{11}\varepsilon_0\,\phi\, I_2 + E_{11}\frac{\phi^3}{2} I_4 \end{aligned} \tag{A-4}$$

where τ is shear stress expressed in the deformed axis, τ_0 is shear stress expressed in the undeformed axis, and I_4 is the fourth moment of area.

The relation between resultant axial force, F and the resultant twisting moment, T, can be found as a nonlinear function of twist rate, ϕ, after substitution of the axial extensional strain, ε_0

$$T = (GJ)\phi + \frac{F}{A}\phi + E_{11}\frac{\phi^3}{2}\left(I_4 - \frac{{I_2}^2}{A}\right) = \left[(GJ) + \frac{F}{A}\right]\phi + E_{11} I_{NL}\phi^3 \tag{A-5}$$

where I_{NL} is the nonlinear term related to the moment of area of the beam.

Finally, the twisting moment can be expressed as the function of the tip twist angle θ

$$T = \left[\frac{(GJ)}{L} + \frac{FI_2}{AL} \right] \theta + \frac{E_{11} I_{NL}}{L^3} \theta^3 = \left(K_{el} + K_F \right) \theta + K_{NL} \theta^3 \qquad \text{(A-6)}$$

where K_{el}, K_F, and K_{NL} represent the elastic torsional stiffness, the apparent torsional stiffness due to axial load and the nonlinear term identified as due to trapeze effect.

REFERENCES

[1] Reichart, G., "Helicopter Vibration Control – A Survey," *Vertica*, Vol. 5, No. 1, 1981, pp. 1-20.

[2] Loewy, R., "Helicopter Vibrations: A Technological Perspective," *Journal of the American Helicopter Society*, Vol. 29, No. 4, October 1984, pp. 4-30.

[3] Fink, D. A., Hawkey, T., Gaudreau, M., Wellman, B., and Ormiston, R., "An electromagnetic actuator for individual blade control," *American Helicopter Society 56th Annual Forum,* Virginia Beach, VA, May 2-4, 2000.

[4] Duvernier, M., Reithler, L., Guerrero, J. Y., and Rossi, R., "Active Control System for a Rotor Blade Trailing-Edge Flap," *Proceedings of the SPIE Smart Structures and Materials 2000 – Smart Structures and Integrated Systems Conference*, Newport Beach, CA, March 6-9, 2000, 3985, pp. 52-61.

[5] Ben-Zeev, O., and Chopra, I., "Advances in the development of intelligent helicopter rotors employing smart trailing edge flaps," *Smart Materials and Structures,* Vol. 5, No. 11, 1996.

[6] Koratkar, N. A., and Chopra, I., "Analysis and testing of a Froude scaled rotor with piezoelectric bender actuated trailing edge flaps," *Journal of Intelligent Material System and Structures,* Vol. 8, No. 555, 1997.

[7] Koratkar, N. A., and Chopra, I., "Design, fabrication and testing of a Mach scaled rotor model with trailing edge flaps," *American Helicopter Society 55th Annual Forum*, Montreal, QC, May 25-27, 1999.

[8] Koratkar, N. A., and Chopra, I., "Wind tunnel testing of Mach-scaled rotor model with trailing edge flaps," *Smart Materials and Structures,* Vol. 10, No. 1, 2001.

[9] Koratkar, N. A., Spencer, M. G., and Chopra, I., "Wind tunnel testing of a Mach-scaled active rotor with trailing edge flaps," *American Helicopter Society 57th Annual Forum,* Washington, DC, May 9-11, 2001.

[10] Fulton, M. V., and Ormiston, R. A., "Small scale rotor experiments with on-blade elevons to reduce blade vibratory loads in forward flight," *American Helicopter Society 54th Annual Forum,* Washington, DC, May 20-22, 1998.

[11] Fulton, M. V., and Ormiston, R. A., "Hover testing of a small scale rotor with on-blade elevons," *Journal of the American Helicopter Society*, Vol. 46, No. 96, 2001.

[12] Spangler, R. L., and Hall, S. R., "Piezoelectric actuators for helicopter rotor control," *31st AIAA Structures, Structural Dynamics, and Materials Conference,* Long Beach, CA, April 2-4, 1990.

[13] Hall, S. R., and Prechtl, E. F., "Development of a piezoelectric servoflap for helicopter rotor control," *Smart Materials and Structures,* Vol. 5, No. 26, 1996.

[14] Bernhard, A., and Chopra, I., "Trailing edge flap activated by a piezo induced bending torsion coupled beam," *Journal of the American Helicopter Society,* Vol. 44, No. 1, 1999.

[15] Bernhard, A., and Chopra, I., "Mach scale design of a rotor with active blade tips," *American Helicopter Society 55th Annual Forum,* Montreal, QC, May 25-27, 1999.

[16] Bernhard A and Chopra I, "Hover test of a Mach-scale rotor-model with active blade tips," *American Helicopter Society 56th Annual Forum,* Virginia Beach, VA, May 2-4, 2000.

[17] Bernhard, A., and Chopra, I., "Analysis of a bending-torsion coupled actuator for a smart rotor with active blade tips," *Smart Materials and Structures*, Vol. 10, No. 35, 2001.

[18] Clement, J. W., Brei, D., Moskalik, A. J., and Barrett, R., "Bench-top characterization of an active rotor blade flap system incorporating C-block actuators," *39th AIAA Structures, Structural Dynamics, and Materials Conference,* Long Beach, CA, April 20-23, 1998.

[19] Clement, J. W., Brei, D., and Barrett, R., "Wind tunnel testing of a high authority, airspeed insensitive, rotor blade flap," *40th AIAA Structures, Structural Dynamics, and Materials Conference,* St. Louis, MO, April 12-15, 1999.

[20] Lee, T., and Chopra, I., "Design and static testing of a trailing edge flap actuator with piezostacks for a rotor blade," *SPIE's Smart Structures and Materials Symposium,* San Diego, CA, March 2-4, 1998.

[21] Lee, T., and Chopra, I., "Design and spin testing of an active trailing edge flap actuated with piezostacks," *40th AIAA Structures, Structural Dynamics, and Materials Conference,* St. Louis, MO, April 12-15, 1999.

[22] Spencer, B. T., and Chopra, I., "Design of a helicopter trailing edge flap with piezoelectric stack actuators," *Smart Structures and Materials – Smart Structures and Integrated Structures,* SPIE Vol. 2717, pp. 120-131, 1996.

[23] Chandra, R., and Chopra, I., "Actuation of trailing edge flap in wing model using piezostack device," *38th AIAA Structures, Structural Dynamics, and Materials Conference,* Kissimmee, FL, April 7-10, 1997.

[24] Lee, T., and Chopra, I., "Wind tunnel test of blade sections with piezoelectric trailing edge flap mechanism," *American Helicopter Society 57th Annual Forum,* Washington, DC, May 9-11, 2001.

[25] Prechtl, E. F., and Hall, S. R., "Design of a high efficiency discrete servoflap actuator for helicopter rotor control," *SPIE's Smart Structures and Materials Symposium,* San Diego, CA, March 2-6, 1997.

[26] Prechtl, E. F., and Hall, S. R., "An X-frame actuator servoflap actuation system for rotor control," *SPIE's Smart Structures and Materials Symposium,* San Diego, CA March 2-6, 1998.

[27] Prechtl, E. F., and Hall, S. R., "Closed-loop vibration control experiments on a rotor with blade mounted actuation," *41st AIAA Structures, Structural Dynamics, and Materials Conference,* Atlanta, GA, April 3-6, 2000.

[28] Straub, F. K., and King, R. J., "Application of smart materials to control of a helicopter rotor," *SPIE's Smart Structures and Materials Symposium,* San Diego, CA, March 2-6, 1996.

[29] Straub, F. K., Ngo, H. T., Anand, V., and Domzalski, D. B., "Development of a piezoelectric actuator for trailing edge flap control of rotor blades," *SPIE's Smart Structures and Materials Symposium,* Newport Beach, CA, March 1-4, 1999.

[30] Straub, F. K., and Charles, B. D., "Comprehensive modeling of rotors with trailing edge flaps," *American Helicopter Society 55th Annual Forum,* Montreal, QC, May 25-27, 1999.

[31] Straub, F. K., Kennedy, D. K., Domzalski, D. B., Hassan, A. A., Ngo, H. T., Anand, V., and Birchette, T., "Smart material actuated rotor technology-SMART," *41st AIAA Structures, Structural Dynamics, and Materials Conference,* Atlanta, GA, April 3-6, 2000.

[32] Wilkie, W. K., Wilbur, M. L., Mirick, P. H., Cesnik, C. E. S., and Shin, S., "Aeroelastic Analysis of the NASA/Army/MIT Active Twist Rotor," *Annual Forum Proceedings – American Helicopter Society*, Vol.1, pp. 545-557, 1999.

[33] Cesnik, C. E. S., and Shin, S., "On the modeling of Integrally Actuated Helicopter Blades," *International Journal of Solids and Structures*, Vol. 38, Nos. 10-13, pp. 1765-1789, March, 2001.

[34] Giurgiutiu, V., "Review of Smart-Materials Actuation Solutions for Aeroelastic and Vibration Control," *Journal of Intelligent Material Systems and Structures*, Vol. 11, No. 7, pp. 524-544, July, 2000.

[35] Rodgers, J. P., and Hagood, N. W., "Preliminary Mach-Scale Hover Testing of an Integral Twist-Actuated Rotor Blade," *Proceedings of SPIE Conference on Smart Structures and Materials*, San Diego, CA, Mach 15, 1998.

[36] Paine, J. S. N., and Chaudry, Z., "The Impact of Amplification on Efficiency and Energy Density of Induced Strain Actuators," *Proceedings of the ASME Aerospace Division*, AD-Vol. 52, pp.511-516, 1996.

[37] Giurgiutiu, V., Chaudry, Z., and Rogers, C., "Stiffness Issues in the Design of ISA Displacement Amplification Devices: Case Study of a Hydraulic Displacement Amplifier," *Proceedings SPIE Smart Structures and Materials, Smart Structures and Integrated Systems*, Vol. 2443, pp. 105-119, 1995.

[38] Glazounov, A. E., Zhang, Q. M., and Kim, C., "A new torsional actuator based on shear piezoelectric response," *SPIE 5th Annual International Symposium on Smart Structures and Materials,* San Diego, CA, March 1-5, 1998.

[39] Glazounov, A. E., Zhang, Q. M., and Kim, C., "Piezoelectric actuator generating torsional displacement from piezoelectric d_{15} shear response," *Applied Physics Letter*, Vol. 72, No. 2526, 1998.

[40] Kim, C., Jessen, T., DeGiorgi, V., Bender, B., Wu, C. C. M., Flippen, D., Lewis, D., Zhang, Q., Mueller, V., Kahn, M., Silberglitt, R,. and Len, L. K., "Composite piezoelectric assemblies for torsional actuator," *Progress Report,* NRL/MR/6380-97-7997, 1997.

[41] Kim, C., Lewis, D., Wu, C. C. M., Kahn, M., Glazounov, A., and Zhang, Q., "High authority piezoelectric torsional actuators," *11th IEEE International Symposium on Applications of Ferroelectrics,* Montreux, Switzerland, August 24-27, 1998.

[42] Kim, C., Glazounov, A. E., Flippen, F. D., Pattnaik, A., Zhang, Q. M., and Lewis, D., "Piezoelectric ceramic assembly tubes for torsional actuators," *SPIE Conference on Smart Materials Technologies,* Newport Beach, CA, March 1-5, 1999.

[43] Kim, C,, Glazounov, A., and Zhang, Q., "Development of piezoelectric ceramic torsional actuators based on shear piezoelectric response and their potential applications," *9th US-Japan Seminar on Piezoelectric Ceramics, Program Summary and Extended Abstract,* Okinawa, Japan, November, 1999.

[44] Newnham, R., and Ruschau, G., "Smart Electroceramics," *The American Ceramic Society Bulletin*, Vol. 75, No. 10, pp. 51-61, October, 1996.

[45] Loewy, Robert G., "Recent developments in smart structures with aeronautical applications," *Smart Materials and Structures*, Vol. 6, pp. 11-42, 1997.

[46] Culshaw, B., "Smart Structures and Materials," *Artech House*, 1996.

[47] Banks, H. Thomas et. al., "Smart material structures : modeling, estimation, and control," *Wiley*, 1996.

[48] Park, C., Waltz, C., Chopra, I., "Bending and torsion models of beams with induced-strain actuators," *Smart Materials and Structures*, Vol. 5, pp. 98-113, 1996.

[49] Moskalik, A. J., and Brei, D., "Quasi-Static Behavior of Piezoelectric C-Block Piezoelectric Actuators," *Journal of Intelligent Material Systems and Structures*, Vol. 8, pp. 571-587, 1997.

[50] Moskalik, A. J., and Brei, D., "Force-Deflection Behavior of Piezoelectric C-Block Actuator Array," *Smart Materials and Structures*, Vol. 8, pp. 531-543, 1999.

[51] Capozzoli, M., Gopalakrishnan, J., Hogan, K., Massad, J., Tokarchik, T., Wilmarth, S., Banks, H. T., Mossi, K. M., and Smith, R. C., "Modeling Aspects Concerning THUNDER Actuators," *Proceedings of the SPIE-The International Society of Optical Engineering*, Vol. 3667, pp. 719-727, 1999.

[52] Shakeri, C., Bordonaro, C. M., Noori, M. N., and Champagne, R., "Experimental Study of THUNDER: A New Generation of Piezoelectric Actuators," *Proceedings of the SPIE-The International Society of Optical Engineering*, Vol. 3675, pp. 63-71, 1999.

[53] Sugawara, Y., Onitsuka, K., Yoshikawa, S., Xu, Q. C., Newnham, R. E., and Uchino, K., "Metal-Ceramic Composite Actuators," *Journal of the American Ceramic Society*, Vol. 75, pp. 996-998, 1992.

[54] Dancila, D. S., and Armanios, E. A., "Large Displacement Piezoelectric Actuator Configurations," *Proceedings of the Adaptive Structures and Material Systems Symposium at the International Mechanical Engineering Congress & Exposition, Winter Annual Meeting of the ASME*, Anaheim, CA, November 15-20, pp. 83-87, 1998.

[55] Dancila, D. S., and Vasilescu, R., "Compact, Large Rotation, Coiled Piezoelectric Actuators – Experimental Validation," *Proceedings of the International Conference on Smart Technology Demonstrators and Devices*, Edinburgh, UK, December 12-14, 2001.

[56] Pearce, D. H., Hooley, A., and Button, T. W., "On Piezoelectric Super-Helix Actuators," *Sensors and Actuators A*, Vol. 100, Issue 2-3, pp. 281-286, 2002.

[57] Pearce, D. H., Seffen, K. A., and Button, T. W., "Net Shape Formed Spiral and Helical Piezoelectric Actuators," *presented at MOLMT Workshop*, UMIST, UK, June 3-6, 2001; published in *Journal of Material Science,* 37, pp. 3117-3122, 2002.

[58] Su, B., Pearce, D. H., and Button, T. W., "Routes to Net Shape Electroceramic Devices and Thick Films," *Journal European Ceramic Society*, Vol. 21, pp. 2005-2009, 2001.

[59] Brei, Diann E., "Force-deflection behavior for C-block piezoelectric actuator architectures," *Proceedings of SPIE - Smart Structures and Materials*, Vol. 2443, pp. 362-373, 1995.

[60] Clement, J. W., Brei, D., and Barrett, R., "Wind tunnel testing of a high authority, airspeed insensitive, rotor blade flap," *40th AIAA Structures, Structural Dynamics, and Materials Conference*, St. Louis, MO, April 12-15, 1999.

[61] Jennifer, L. Pinkerton and Robert, W. Moses, "A Feasibility Study To Control Airfoil Shape Using THUNDER," *NASA Technical Memorandom 4767*, November, 1997.

[62] Onitsuka, K., Dogan, A., Tressler, J. F., Xu, Q., Yoshikawa, S., and Newnham, R., "Metal-Ceramic Composite Transducers, the Moonie," *Journal of Intelligent Material Systems and Structures*, Vol. 6, pp. 447-455, July, 1995.

[63] Seffen, K. A., and Toews, E., "Hyperhelical Actuators: Coils and Coiled-Coils," *12th AIAA/ASME/AHS Adaptive Structures Conference*, Palm Springs, CA, April 19-22, 2004.

[64] Barrett, R., “Intelligent rotor blade and structures using directionally attached piezoelectric crystals,” *MS Thesis*, University of Maryland, 1990.

[65] Chopra, I. and Samak, D. K., "Development of an Intelligent Rotor," *Proceedings of the ADPA/AIAA/ASME/SPIE Conference on Active Materials and Adaptive Structures*, Alexandria, VA, November 4-8, 1991.

[66] Nitzsche, F., and Breitbach, E., “A study on the feasibility of using adaptive structures in the attenuation of vibration characteristics of rotary wings,” *Proceedings of the 33rd AIAA SDM Conference*, Dallas, TX, pp. 1391-1402, April 13-15, 1992.

[67] Strehlow, H., and Rapp, H., “Smart materials for helicopter rotor active control,” *Proceedings of the AGARD/SMP Specialist’s Meeting on Smart Structures for Aircraft and Spacecraft*, Lindau, pp. 5.1-5.16, 1992.

[68] Fabunmi, J. A., “Control of helicopter rotor blade aerodynamics,” *NASA CR 4350*.

[69] Ormiston, R. A., “Can Smart materials make helicopters better?,” Proceedings of the 4th Workshop on Dynamics and Aeroelastic Stability Modeling of Rotorcraft Systems, 1991.

[70] Walz, C., and Chopra, I., “Design and testing of a helicopter rotor model with smart trailing edge flaps,” *Proceedings of the 35th AIAA/ASME/ASCE/AHS/ASC Structures, Structural Dynamics and Materials Conference and AIAA/ASME/AHS Adaptive Structures Forum*, Hilton Head, SC, April 18-20, 1994.

[71] Giurgiutiu, V., Rogers, C. A., and McNeil, S., “Static and dynamic testing of large-amplitude rotary induced strain (Laris Mk2) actuator,” *Journal of Intelligent Material Systems and Structures*, Vol. 8, pp. 502-512, June, 1997.

[72] Milgram, J., and Chopra, I., “A parametric design study for actively controlled flaps,” *Journal of the American Helicopter Society*, Vol. 43, pp. 110-119, April, 1998.

[73] Bend, A. A., and Hagood, N. W., “Improved Performance in Piezoelectric Fiber Composites Using Interdigitated Electrodes,” *Presented at the 1995 SPIE North American Conference on Smart Structures and Materials*, San Diego, CA, February 28-March 2, 1995.

[74] du Plessis, A. J., and N. W. Hagood, “Performance Investigation of Twist Actuated Single Cell Composite Beams for Helicopter Blade Control,” *6th International Conference on Adaptive Structures Technolog*y, Key West, FL, May 20-22, 1995.

[75] Derham, R. C., and Hagood, N. W., "Rotor design using smart materials to actively twist blades", *AHS 52nd Annual Forum*, Washington, DC, June 4-6, 1996.

[76] Rodgers, J. P., and Hagood, N. W., and Weems, D. B., "Design and Manufacture of an Integral Twist Actuated Rotor Blade," *38th AIAA/ASME/AHS Adaptive Structures Forum,* Kissimmee, FL, April 7-10, 1997.

[77] Rodgers, J. P., and N. W. Hagood, "Design of an Integral Twist-Actuated Rotor Blade for Individual Blade Control," *PhD. Thesis*, Massachusetts Institute of Technology, October, 1998.

[78] Stroub, R. H., "An Analytical Investigation of the Free-Tip Rotor for Helicopters," *NASA Report*, N82-18179, 1982.

[79] Stroub, R. H., Young, Larry A., Keys, Charles N., and Cawthorne, Matthew H., "Free-Tip Rotor Wind Tunnel Test Results," *Proceedings of 41st AHS Annual Forum of the American Helicopter Society,* Ft. Worth, Texas, May 9-11, 1985.

[80] Chopra, I., "Dynamic Analysis of Constant-Lift and Free-Tip Rotors," *Proceedings of AIAA Dynamic Specialists Conference,* Atlanta, Georgia, April 6-10, 1981.

[81] De Goeij, W.C., Van Tooren, M. J. L., and Beukers, A., "Implementation of bending-torsion coupling in the design of a wind-turbine rotor-blade," *Applied Energy,* Vol. 63, pp. 191-207, 1999.

[82] Kosmatka, J. B., "Extension-Bend-Twist Coupling Behavior of Nonhomogeneous Anisotropic Beams with Initial Twist," *AIAA Journal*, Vol. 30, No. 2, pp. 519-527, February, 1992.

[83] Armanios, E. A., Makeev, A., and Hooke, D. A., "Finite-Displacement Analysis of Laminated Composite Strips with Extension-Twist Coupling", *Journal of Aerospace Engineering*, Vol. 9, No. 3, pp. 80-91, July, 1996.

[84] Dancila, D. S., Kim, I. B., and Armanios, E. A., " Star-Shape Cross-Section Extension-Twist-Coupled Composite Beams for Rotorcraft Applications," *Proceedings of 54th AHS Annual Forum and Technology Display, American Helicopter Society Inc.,* pp 1044-1049, Washington, DC, May 20-22, 1998.

[85] Kim, I. B., Dancila, D. S., and Armanios, E. A., "Design, Manufacturing and Testing of Elastically Tailored Composite Star Beam Configurations," *Proceedings of the 44th AIAA/ASME/ASCE/AHS/ASC Structures, Structural Dynamics, and Materials Conference and Exhibit,* Norfolk, VA, April 7-10, 2003.

[86] Ha, K., and Dancila, D. S., "Characterization of Modified Star Shape Cross-Sectional Beam Configurations with Rotorcraft Applications," *44th AIAA/ASME/ASCE/AHS Structures, Structural Dynamics, and Material Conference*, Norfolk, VA, April 6-9, 2003.

[87] Vasilescu, R., and Dancila, D. S., "Modeling and Analysis of Active Flap Using Coiled Bender Piezoelectric Actuators," *Journal of Intelligent Material Systems and Structures*, Vol. 15, No. 9-10, pp. 783-792, 2004.

[88] Hibbit, Karlsson and Sorensen, Inc., "ABAQUS/Standard User's manual," 2002.

[89] Bauchau, O.A., "Computational Schemes for Flexible, Nonlinear Multi-Body Systems," *Multibody System Dynamics*, Vol. 2, pp. 165-225, 1998.

[90] Kim, Inn B., "Development and Analysis of Elastically Tailored Composite Star Shape Beam Sections," *Ph. D. Thesis,* Georgia Institute of Technology, 2005.

[91] Leishman, J. Gordon, "Principles of Helicopter Aerodynamics," *Cambridge*, 2000.

VITA

Kwangtae Ha was born in Chinju, Korea on April 6, 1974. He received his Bachelor of Science Degree in Mechanical/Automotive Engineering from Hanyang University (Seoul) in 1996. He also received Master of Science in Automotive Engineering from Hanyang University in 1998. After graduation, he performed compulsory military service for 2 years. He subsequently attended Georgia Institute of Technology in Atlanta, Georgia, earning a Master of Science degree in Aerospace Engineering in May 2004. While at Georgia Tech, he married Simbackhwa Lee in 2004 and his son, Gundam, will be born on December 2005.